Conserving approximations for strongly fluctuating electron systems. II. Numerical results and parquet extension

N. E. Bickers
Department of Physics, University of Southern California, Los Angeles, California 90089

S. R. White
Department of Physics, University of California, Irvine, California 92717
(Received 23 October 1990)

We describe an iterative technique for solution of the de Dominicis–Martin parquet equations for lattice electrons and state the relationship of this approach to conserving extensions of Hartree-Fock theory. We propose a physically motivated and computationally feasible pseudopotential approximation, which allows the solution of the parquet equations for the two-dimensional Hubbard model. We present calculations of static and dynamic Hubbard-model correlation functions based on the pseudopotential parquet and a simpler conserving approximation. For a wide parameter range the pseudopotential parquet results are in nearly quantitative agreement with finite-lattice quantum Monte Carlo results.

I. INTRODUCTION

Strongly correlated electron systems, including the heavy-electron metals[1] and the high-temperature oxide superconductors,[2,3] have been studied using a wide variety of theoretical techniques. Finite-temperature studies have generally relied on some form of mean-field theory, whether in the weak-[4,5] or strong-coupling[6,7] limit. Mean-field theories ignore the effect of fluctuations, which are expected to be particularly important in regions of competing order (e.g., antiferromagnetism and superconductivity). In order to incorporate the detailed effects of fluctuations, approximations which extend mean-field theory are required. A powerful approach is provided by direct quantum Monte Carlo (QMC) simulation of correlation functions.[8–10] This approach has a number of limitations, however; in any case, more analytical techniques provide a useful complement to QMC.

In an earlier paper[11] (hereafter referred to as I) we developed the formalism for a conserving extension of mean-field theory for lattice electrons. The extension, which we called the fluctuation exchange (FLEX) approximation, self-consistently incorporates the effects of a large class of magnetic, density, and particle-pair fluctuations. This approach may be viewed diagrammatically as an all-orders resummation of perturbation theory about the weak-coupling, or band, limit. A similar approach has been suggested by Ruckenstein and Schmitt-Rink[12] for treating fluctuations in the strong-coupling limit.

In this paper we enlarge our discussion of extensions of mean-field theory to include additional self-consistent-field (SCF) approximations. In particular we consider the group of approximations generally referred to as parquet summations. This class of approximations was first considered systematically in a condensed-matter context by de Dominicis and Martin[13] in their papers on renormalization in quantum statistical mechanics. Approximate parquet solutions for ^{3}He and nuclear matter have been studied since the work of Babu and Brown.[14–16]

We show that the FLEX approximation may be viewed as the first step in an iterative solution of the parquet equations for a lattice system. Subsequent iterations improve the consistency of the particle-hole and particle-particle scattering vertices which appear in complete two-particle propagators and in the single-particle self-energy. We introduce a physically motivated pseudopotential approximation which provides a feasible means to solve approximately the full parquet equations.

After developing the necessary parquet formalism in Sec. II, we go on to calculate one- and two-particle Hubbard model correlation functions within the FLEX and pseudopotential parquet approximations in Sec. III. Wherever possible we compare our results directly with QMC simulations for finite-lattice systems. We argue that the pseudopotential parquet provides results with nearly quantitative accuracy throughout the intermediate coupling regime. Finally, in Sec. IV, we summarize our conclusions on the validity of these SCF approaches and comment on the outlook for improved solutions of the lattice parquet equations.

II. PARQUET EQUATIONS

In Sec. II A we discuss the derivation of formal parquet equations and their relationship to the FLEX approximation of I. In Sec. II B we discuss a pseudopotential approximation that allows an explicit, but approximate, parquet solution.

A. Formal derivation

The approximations described in I[11] are guaranteed to satisfy a set of local conservation laws and to be internally self-consistent.[17,18] The preservation of conservation laws is crucial for obtaining a reasonable description of

low-energy dynamics and transport. On the other hand, these approximations do not satisfy a basic symmetry relation implied by the Pauli exclusion principle: the full particle-hole or particle-particle vertex Γ connecting two states must be invariant under exchange, or crossing, symmetry. In diagrammatic terms the exchange operation amounts to twisting the external legs of the vertex to represent one of three possible channels. The channels are characterized by the various ways in which the full vertex may be decomposed as a ladder sum with irreducible rungs. The three possible decompositions are shown in Fig. 1. Each Φ-derivable[18] approximation of the type described in I generates specific expressions for the irreducible vertices $\Gamma^{\rm ph}$ ($=\bar{\Gamma}^{\rm ph}$) and $\Gamma^{\rm pp}$. The three different summations which result from these irreducible vertices are clearly not consistent with crossing symmetry. For example, at Hartree-Fock level the transverse spin vertex $\Gamma^{\rm ph}_m$ in the (12)-channel takes the form in Fig. 2(a). By twisting the external legs (or, alternatively, turning the diagram on its side) the corresponding contribution to $\bar{\Gamma}^{\rm ph}_{+-}$ is found to be that in Fig. 2(b). This diagram is irreducible in the (13)-channel, i.e., it is a separate contribution to $\bar{\Gamma}^{\rm ph}_{+-}$ not present at Hartree-Fock level. The same problem occurs when Fig. 2(a) is used to generate contributions to the particle-particle vertex $\Gamma^{\rm pp}_{+-}$ [Fig. 2(c)].

The lack of crossing symmetry at Hartree-Fock level and in any higher-order Φ-derivable approximation limits the quantitative accuracy of one- and two-particle correlation functions. The problem is the following: the criterion of Φ derivability ensures only that a consistent expression for the one-particle potential Σ appears at all points in a calculation; it does not ensure that a consistent expression for the two-particle potential $\Gamma^{\rm ph}$ ($\Gamma^{\rm pp}$) appears at all points. In particular, within the FLEX approximation of I, the two-particle potential which enters the fluctuation propagator in Σ is always the bare interaction v; on the other hand, when susceptibilities are calculated, the two-particle potentials incorporate fluctuation effects from crossed channels. If fluctuations *reduce* the attractive interaction in a singular channel from its bare value, the self-energy Σ calculated with the bare potential overestimates the effect of interactions (roughly speaking, too much electronic density is repelled from the Fermi level). The only way to eliminate effects

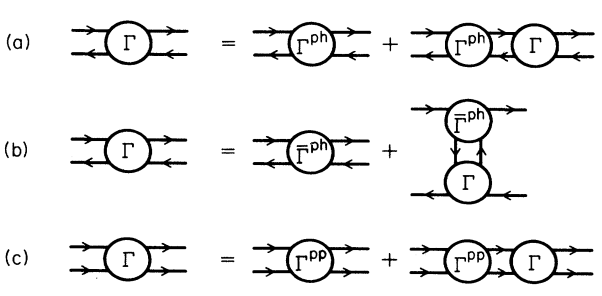

FIG. 1. Possible reductions of the full two-particle scattering vertex Γ. (a) Particle-hole reduction based on $\Gamma^{\rm ph}$. (b) Crossed-channel particle-hole reduction based on $\bar{\Gamma}^{\rm ph}$. (c) Particle-particle reduction based on $\Gamma^{\rm pp}$.

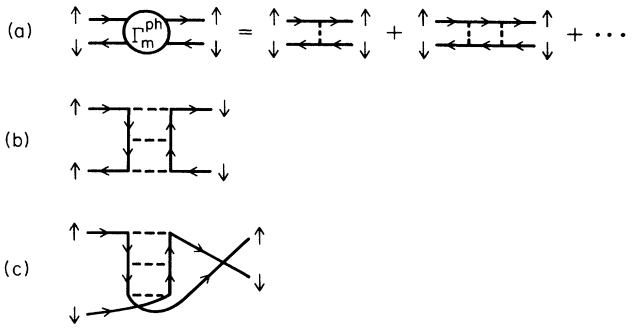

FIG. 2. Illustration that the Hartree-Fock approximation is not crossing symmetric. (a) Hartree-Fock approximation for the complete transverse magnetic vertex. (b) Contribution to the longitudinal magnetic and density vertices from applying the crossing operation to (a). (c) Contribution to the particle-particle vertex from applying the crossing operation to (a).

of this type is to arrive at a self-consistent expression for the two-particle potentials $\Gamma^{\rm ph}$, $\bar{\Gamma}^{\rm ph}$, and $\Gamma^{\rm pp}$ wherever they occur in an approximate theory. This includes occurrences in the self-energy and in susceptibilities (which may be viewed as momentum- and frequency-averaged matrix elements of the full vertex Γ).

The formal means for generating self-consistent expressions for two-particle potentials was developed in the context of continuum Bose and Fermi systems by de Dominicis and Martin[13] in the early 1960's. Since that time this approach has been applied extensively in Fermi liquid studies of ^{3}He and nuclear matter.[14–16] For normal Fermi systems it is necessary to solve a set of coupled nonlinear equations for the three irreducible vertices $\Gamma^{\rm ph}$, $\bar{\Gamma}^{\rm ph}$, and $\Gamma^{\rm pp}$.[19] These equations take the diagrammatic form shown in Fig. 3. Note that each vertex Γ represents a matrix in space, time, and spin: within a single-particle labeling scheme the matrix elements take the form $\Gamma_{ll'}$, where the compound index $l=\{r_1t_1\sigma_1,r_2t_2\sigma_2\}$.

The parquet equations may be motivated formally by iteratively improving the zeroth-order approximation

$$\Gamma=\Lambda^{\rm irr}\ , \tag{2.1}$$

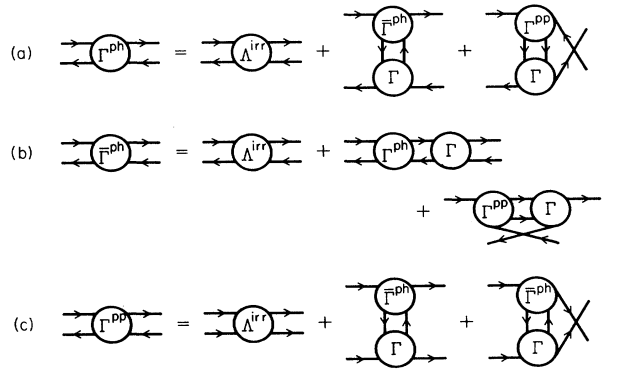

FIG. 3. Parquet equations for irreducible vertices in the three alternative channels. (a) $\Gamma^{\rm ph}$, (b) $\bar{\Gamma}^{\rm ph}$, (c) $\Gamma^{\rm pp}$.

where $\Lambda^{\rm irr}$ is irreducible in all three scattering channels. The simplest choice for the fully irreducible vertex is just

$$\Lambda^{\rm irr}=v\ , \tag{2.2}$$

where both the direct and exchange contributions to the bare potential are implied. As discussed in I, this choice generates the RPA two-particle propagators and susceptibilities. The next contribution to $\Lambda^{\rm irr}$ for a general potential is the envelope graph shown in Fig. 4. Throughout this paper we concentrate on the parquet generated by the simpler choice of Eq. (2.2).

As mentioned above, non-Hartree-Fock contributions to $\Gamma^{\rm ph}$, $\bar{\Gamma}^{\rm ph}$, and $\Gamma^{\rm pp}$ may be generated by applying the crossing operation to the three Hartree-Fock ladder approximations for Γ. It is easy to check that this procedure exactly reproduces the one-fluctuation-exchange contributions [Fig. 5(a)] to $V^{(\rm pp)}$ and $V^{(\rm ph)}$ found in I; the Aslamazov-Larkin (AL) graphs,[20] which necessarily accompany the one-fluctuation-exchange graphs in a strictly Φ-derivable approximation[11,18] [Fig. 5(b)], appear as a small fraction of the total set of contributions in the *next* iteration of the crossing process. Note that the approximate form for the irreducible vertices after each iteration may be obtained directly from the one-fluctuation-exchange expressions in I if the coupling matrices v_r are replaced by V_r from the previous iteration; with this modification (and the omission of the AL graphs, which close the approximation in the Baym-Kadanoff sense after one iteration), the notation of I may be preserved intact. Assuming the iterative improvement of the irreducible vertices by the crossing operation converges, this process yields an explicit solution of the parquet equations with full crossing symmetry. The Hartree-Fock and FLEX approximations may be viewed as zeroth- and first-order elements in a hierarchy of successive approximations to the full parquet solution. Note, however, that the full parquet is not guaranteed to satisfy the rigorous conservation laws and thermodynamic self-consistency criteria of the Baym-Kadanoff approximations.

The irreducible vertices generated by iterative solution of the parquet equations must appear in the calculation of the self-energy. Conversely, the self-energy must appear in all single-particle propagators within the expressions for $\Gamma^{\rm ph}$, $\bar{\Gamma}^{\rm ph}$, and $\Gamma^{\rm pp}$. This means that the set of coupled equations in Figs. 3 must be supplemented by one additional equation representing the self-energy. This equation has the diagrammatic form shown in Fig. 6(a), where spin labels are suppressed. As in the derivation of the FLEX approximation in I, some care is required to prevent double-counting of low-order terms. For example, the contribution to Γ shown in Fig. 6(b) is

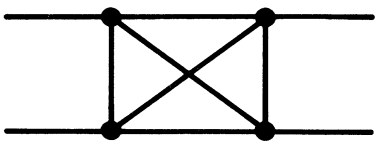

FIG. 4. First contribution to the fully irreducible vertex $\Lambda^{\rm irr}$ beyond $\Lambda^{\rm irr}=v$. The elementary vertices are represented here by solid dots, rather than dashed lines.

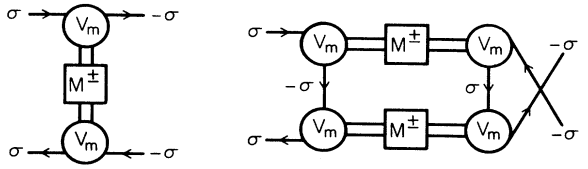

FIG. 5. Examples of one-fluctutation-exchange and Aslamazov-Larkin (AL) graphs. (a) One-fluctuation-exchange contribution to the longitudinal magnetic and density vertices. (b) AL contribution to the longitudinal magnetic and density vertices.

irreducible in the (12) particle-hole channel and might be included as the first rung in a ladder of irreducible vertices in this channel. This contribution is generally not irreducible in the other two channels, however, and must not be double-counted when ladder sums are performed in those channels. The simplest way to prevent double-counting is to separate out the term of $O(v\Lambda^{\rm irr})$ for special treatment [in analogy with the treatment of the term of $O(v^2)$ in I], then to commence ladder sums based on the irreducible vertices at $O[v(\Gamma_r)^2]$. The self-energy then takes the form shown in Fig. 6(c).

The non-Hartree-Fock contributions may be written out explicitly as follows:

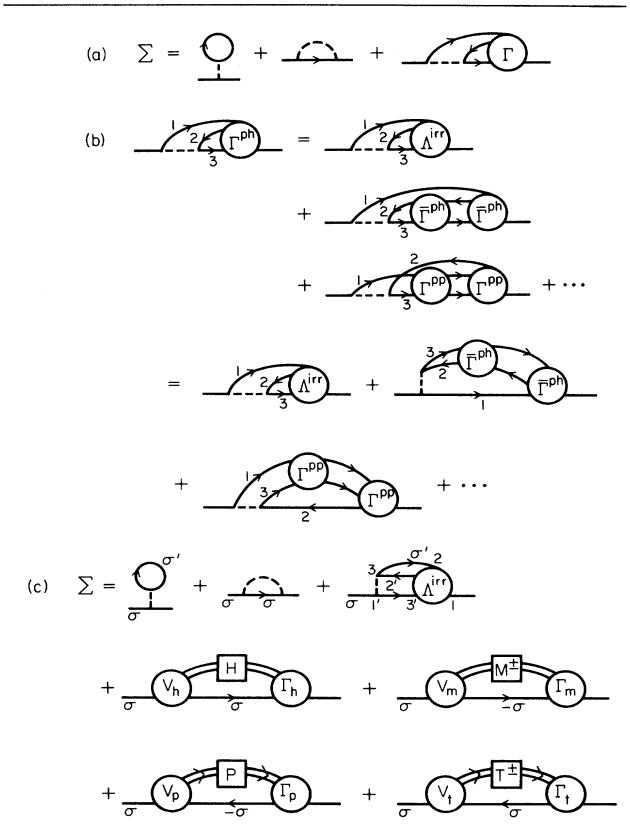

FIG. 6. Self-energy diagrams for parquet approximations. (a) Formal representation of the self-energy Σ in terms of the full two-particle vertex Γ. (b) Diagrams which potentially give rise to double counting in Σ. (c) Parquet approximation for the self-energy in terms of irreducible vertices Γ_r.

$$\Sigma_\sigma(11')=\Sigma_\sigma^{(2)}(11')+\Sigma_\sigma^{(\mathrm{ph})}(11')+\Sigma_\sigma^{(\mathrm{pp})}(11') , \tag{2.3a}$$

$$\Sigma_\sigma^{(2)}(11')=-\beta\sum_{22'33'}\Lambda^{\mathrm{irr}}_{12,2'3'}v(1'-3)[2G(3'-1')G(2-3)G(3-2')-G(3'-3)G(3-2')G(2-1')] , \tag{2.3b}$$

$$\Sigma_\sigma^{(\mathrm{ph})}(11')=\beta\sum_{23}G(2-3)[\tfrac{1}{2}v_d(D-\bar{D})\Gamma_d+\tfrac{3}{2}v_m(M-\bar{M})\Gamma_m]_{12,31'} , \tag{2.3c}$$

$$\Sigma_\sigma^{(\mathrm{pp})}(11')=-\beta\sum_{23}G(3-2)[v_s(S-\bar{S})\Gamma_s+3v_t(T-\bar{T})\Gamma_t]_{12,31'} . \tag{2.3d}$$

Here, as in I, the $\bar{R}$ matrices are uncorrelated fluctuation propagators which include single-particle self-energies, but omit the vertices Γ_r; and now

$$R(q)=\bar{R}(q)[1+\beta\Gamma_r(q)\bar{R}(q)]^{-1} , \tag{2.4}$$

i.e., the bare interaction v_r is replaced by Γ_r in each channel. By introducing subtracted propagators $R-\bar{R}$, the terms of $O(v\Gamma_r)$ which would lead to double-counting are explicitly removed. Note that in an iterative solution the Γ_r in Eq. (2.3) are vertices determined at the end of the *preceding* iteration.

In the simplest approximation

$$\Lambda^{\mathrm{irr}}_{12,2',3'}=v(1-2)\delta(2-2')\delta(1-3') , \tag{2.5}$$

and the expression for $\Sigma^{(2)}$ reduces to that found in I. In writing Eq. (2.3b) it has been assumed that the approximation for Λ^{irr} is itself crossing-symmetric and spin-independent, i.e., of the same form as the bare interaction v. In practice we shall adopt the approximation in Eq. (2.5), so that $\Sigma^{(2)}$ has exactly the same structure as in I.

If v_r vanishes for a particular channel (as, e.g., v_t does in the Hubbard model), then contributions from that channel drop out of Eq. (2.3). This does not mean that triplet-pair fluctuations are absent from the self-energy in the Hubbard model parquet; instead, they appear in the irreducible vertices for other channels. They could be made to appear explicitly if subtractions were made elsewhere to prevent double counting.

B. Pseudopotential approximation

The equations represented diagrammatically in Figs. 3 and 6 constitute the full parquet approximation. For an isolated nonmagnetic impurity in a sea of conduction electrons these equations may be solved analytically[21] to extract the x-ray edge singularity. In one dimension the same equations constitute the basis for the renormalization-group analysis of zero-temperature singularities in Green's functions and susceptibilities.[22] Considerably less is known about the behavior of the equations in dimensions $d\geq 2$; however, in three dimensions approximate solutions of the parquet equations have been studied extensively in the theory of Fermi liquids such as ^{3}He and nuclear matter.[14–16]

Lattice systems are in some sense more amenable to solution than continuum systems: momentum sums are restricted to a Brillouin zone, rather than allowed to range throughout all space. Despite this advantage, a full solution of the parquet equations for a square or cubic lattice appears presently out of reach. A limiting computational factor is the inversion of large matrices necessary to perform the ladder sums in fluctuation propagators beyond Hartree-Fock level.

In this section we develop an approximate solution of the parquet equations motivated by a physical idea of Berk and Schrieffer[23] from the 1960s. In their paper on spin fluctuations and superconductivity Berk and Schrieffer employed renormalized RPA propagators, within which the bare on-site Coulomb interaction U was replaced by a smaller effective interaction $\bar{U}$. This approximation was motivated by the observation that correlation effects (in particular, the repeated singlet-pair scattering process represented in Fig. 7) tend to reduce the effective interaction in the magnetic channel. Such effects are included in the first iteration of the parquet equations beyond the FLEX level of I. The frequency and momentum dependence of the renormalized magnetic vertex may be quite complicated; however, Berk and Schrieffer assumed the effect could be well represented by simply introducing a new instantaneous on-site interaction $\bar{U}$. The size of the renormalization may be estimated by choosing particular values for the incoming and outgoing frequency and momentum. We shall call vertex approximations of this form "pseudopotentials" in analogy with the technique used to eliminate core-electron states in atomic calculations. As in the atomic case, we shall choose pseudopotentials which preserve a particular matrix element of the full vertex (in our case, a susceptibility), then examine the transferrablity of the approximation for other matrix elements.

The use of pseudopotentials of this type should be reasonable when vertex renormalization effects are caused by fluctuations which act over a broad range of frequencies and momenta. On the other hand, a more precise treatment of frequency and momentum dependence is certainly required for the analysis of possible Fermi surface singularities[21] in the $T\rightarrow 0$ limit. In the nearly-half-filled Hubbard model, where large-Q spin fluctuations play a dominant role, the most important vertex renormalization (at least at intermediate tempera-

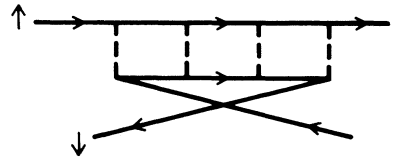

FIG. 7. Renormalization of the irreducible transverse magnetic vertex by repeated scattering in the singlet particle-particle channel.

tures) is the change in the magnetic vertex due to nonsingular singlet-pair and density fluctuations. A pseudopotential treatment seems particularly well suited to this case (as noted by Berk and Schrieffer in a more phenomenological context).

In general, three separate pseudopotentials must be introduced to describe the irreducible vertices in a Hubbard-like model. These pseudopotentials represent scattering in the magnetic (Γ_m), density (Γ_d), and singlet-pair (Γ_s) channels. No triplet-pair vertex appears since the amplitude for instantaneous occupation of a site by a spin triplet vanishes. Our procedure for iterating the parquet equations with pseudopotentials is as follows. (a) Calculate full frequency- and momentum-dependent vertices within the FLEX approximation of I (excluding the AL diagrams); (b) using these vertices calculate a susceptibility corresponding to each of the three channels. A choice of total frequency Ω and total momentum $\mathbf{Q}$ must be made for each channel. For the two-dimensional Hubbard model we have in all cases taken $\Omega=0$; we have chosen $\mathbf{Q}=(\pi,\pi)$ for the magnetic and density channels and $\mathbf{Q}=0$ for the singlet-pair channel. (c) Introduce pseudopotential vertices U_m, U_d, and U_s by demanding

$$\chi_r(\mathbf{Q},\Omega)=\frac{\bar{\chi}_r(\mathbf{Q},\Omega)}{1\pm U_r\bar{\chi}_r(\mathbf{Q},\Omega)} . \tag{2.6}$$

Here χ_r is the result from using the full frequency- and momentum-dependent vertices, while $\bar{\chi}_r$ is the corresponding uncorrelated susceptibility, i.e., the result obtained using fully dressed single-electron propagators, but omitting the vertex Γ_r (see Fig. 8). The sign in the denominator is minus for the magnetic channel and plus for the other two. Note that at Hartree-Fock level

$$U_d=U_s=U_m=U . \tag{2.7}$$

At higher iteration levels the pseudopotentials are, in general, all different. Note, however, that at half-filling particle-hole symmetry implies $U_d=U_s$ if the pseudopotentials are referred to $\mathbf{Q}=(\pi,\pi)$ for the density channel and $\mathbf{Q}=0$ for the singlet. (d) Recompute the self-energy Σ replacing the bare Hubbard interaction U with the pseudopotential approximations for the vertices in each fluctuation channel. It is at this point that a nonrigorous approximation is first introduced. The approximate self-energy takes the form

$$\Sigma_\sigma(k)=\frac{1}{N}\sum_q [G(k-q)V^{(2)}(q)+G(k-q)V^{(\mathrm{ph})}(q) +G(-k+q)V^{(\mathrm{pp})}(q)] , \tag{2.8}$$

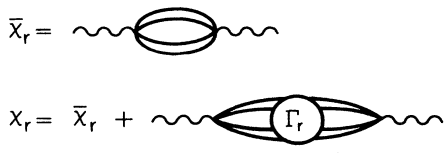

FIG. 8. Uncorrelated and vertex-corrected susceptibilities $\bar{\chi}_r$ and χ_r.

where

$$V^{(2)}(q)=U^2\chi_{\mathrm{ph}}(q) , \tag{2.9a}$$

$$V^{(\mathrm{ph})}(q)=\tfrac{1}{2}UU_d\chi_{\mathrm{ph}}(q)\left[\frac{1}{1+U_d\chi_{\mathrm{ph}}(q)}-1\right] +\frac{3}{2}UU_m\chi_{\mathrm{ph}}(q)\left[\frac{1}{1-U_m\chi_{\mathrm{ph}}(q)}-1\right] , \tag{2.9b}$$

$$V^{(\mathrm{pp})}(q)=-UU_s\chi_{\mathrm{pp}}(q)\left[\frac{1}{1+U_s\chi_{\mathrm{pp}}(q)}-1\right] . \tag{2.9c}$$

This simple form follows immediately by replacing the full vertices Γ_r with pseudopotentials in Eq. (2.3). The approximation of instantaneous on-site pseudopotentials allows the fluctuation propagators to be calculated explicitly by summing geometric series, as in the RPA. More generally, these propagators can only be calculated by numerical matrix inversion: it is this step which makes full solution of the parquet equations unfeasible at present (at least in two and three dimensions). (e) After converging the self-energy recompute the vertices Γ_r using the pseudopotentials U_r in crossed channels. (f) Iterate steps (a–e) until the pseudopotentials (and the self-energy) converge. (g) Calculate detailed frequency- and momentum-dependent correlation functions using the resulting full vertices Γ_r. Note that it is crucial to use the full vertices rather than the pseudopotentials to calculate functions like the singlet d-wave and triplet p-wave pair susceptibilities.

The pseudopotential approximation described above is nonrigorous and precludes the treatment of a number of interesting problems. In particular, triplet fluctuations (which appear only in crossed-channel contributions to the Hubbard self-energy when the representation of Fig. 6 is employed) are omitted completely from the iterative process (see Fig. 9). So long as these fluctuations are small and nonsingular, this omission is reasonable. However, in cases where a triplet-pairing instability is possible (as in the low-density limit of the Hubbard model), these fluctuations may strongly affect both the self-energy and the irreducible vertices in crossed channels. The restric-

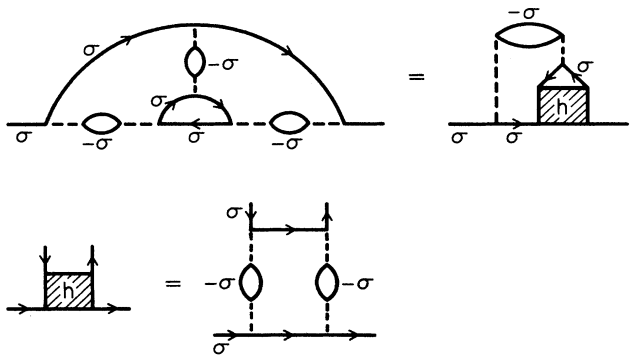

FIG. 9. Rewriting of a triplet fluctuation contribution to the self-energy in terms of longitudinal magnetic and density fluctuations. The shaded vertex "h" represents a contribution to either the magnetic or density vertices (i.e., Γ_m or Γ_d).

tion to instantaneous on-site pseudopotentials is then unsuitable. The same problem arises whenever extended-range fluctuations play an important quantitative role; e.g., a more complicated approximation would be necessary to treat renormalization effects due to d-wave singlet-pair fluctuations. We comment briefly on the form of possible extended-range pseudopotentials in Sec. IV.

III. RESULTS

In this section we present results obtained for the Hubbard model using the FLEX approximation of I and the pseudopotential parquet approximation discussed in Sec. II B. We begin with a detailed examination of technical points involved in the solution, including effects of a finite momentum mesh, finite frequency cutoffs, and the quantitative importance of the Aslamazov-Larkin[11,19] graphs. We go on to compare results obtained using the FLEX and parquet approximations with results from finite-lattice QMC simulations. Properties discussed include the single-particle Green's function; particle-hole and particle-particle susceptibilities; and equal-time two-particle correlation functions.

In the QMC calculations[8–10] used for comparison below, we have introduced auxiliary fields via Hubbard-Stratonovich transformations to put the Boltzmann weight factor $\exp(-\beta H)$ in single particle form, then summed over the auxiliary fields using Monte Carlo. The calculations yield finite-temperature, imaginary-time one- and two-particle correlation functions. The results are exact for the finite lattices studied, except for the presence of (a) statistical errors and (b) errors due to finite discretization in the imaginary time direction. The statistical errors in the calculations reported below are generally comparable or smaller in size than the symbols in the figures; the discretization errors are typically on the order of a few percent. Both types of error can be systematically reduced. The calculations use matrix stabilization techniques[9] to reach lower temperatures; however, minus sign problems[24] still limit the temperatures that can be reached (except at half-filling).

A. Finite discretization in momentum space

Error in SCF calculations of infinite-lattice properties arises from (a) the SCF approximation itself and (b) the numerical approximations necessary to solve a specified set of SCF equations. In this and the following two sections we consider error arising from the second source.

In order to convert equations involving Brillouin zone integrations to tractable matrix equations, a momentum mesh must be introduced. Ideally a variable mesh should be employed to emphasize Fermi-surface structure while avoiding needlessly detailed treatment of the high- and low-momentum regions. We have, however, to this point employed square meshes which divide the Brillouin zone into uniform blocks. Each block consists of an infinite set of distinct states represented by a single $\mathbf{k}$ point. The situation is different in true finite system calculations, where $\mathbf{k}$ points represent single states, whose occupancy is governed by the Pauli exclusion principle.

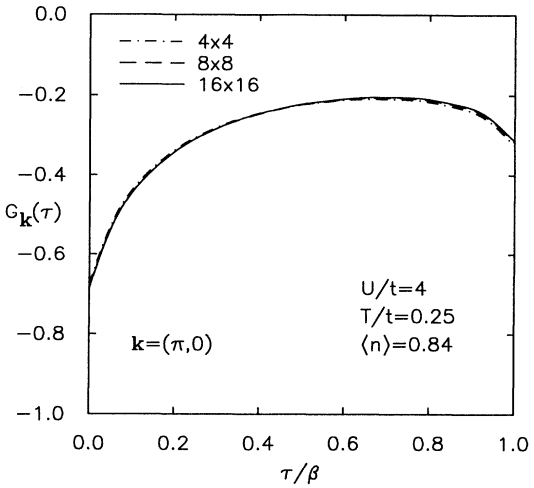

FIG. 10. Dependence of the FLEX Green's function $G_{\mathbf{k}}(\tau)$ on discretization scale. Results are shown for 4^2, 8^2, and 16^2 meshes at the intermediate temperature $T/t=0.25$. The mean density is $\langle n \rangle = 0.84$.

The quantitative error from solving SCF equations on a finite mesh varies with the temperature scale. We illustrate the effect of discretization within the FLEX approximation in Figs. 10–13. Results are shown for the imaginary-time Green's function $G_{\mathbf{k}}(\tau)$, $\mathbf{k}=(\pi,0)$; and the occupancy factor $n_{\mathbf{k}}=\langle c_{\mathbf{k}}^{\dagger}c_{\mathbf{k}} \rangle$. The mean density is fixed at $\langle n \rangle = 0.84$, and $U/t=4$. In Figs. 10 and 11 $T/t=0.25$, while in Figs. 12 and 13 $T/t=0.05$. The Green's function is calculated using the formula

$$G_{\mathbf{k}}(\tau)=\sum_{\omega_n=-\Omega}^{\Omega} e^{-i\omega_n\tau}[G_{\mathbf{k}}(i\omega_n)-G_{\mathbf{k}}^0(i\omega_n)] + G_{\mathbf{k}}^0(\tau)\ , \tag{3.1}$$

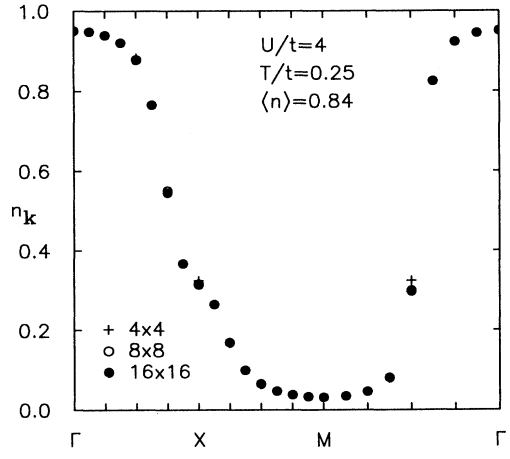

FIG. 11. Dependence of the FLEX occupancy factor $n_{\mathbf{k}}$ on discretization scale. Results are shown for the triangular contour $\Gamma \rightarrow X \rightarrow M \rightarrow \Gamma$ in the 2D Brillouin zone. Parameters are as in Fig. 10. Note the development of an apparent Fermi surface discontinuity along ΓX and $M\Gamma$.

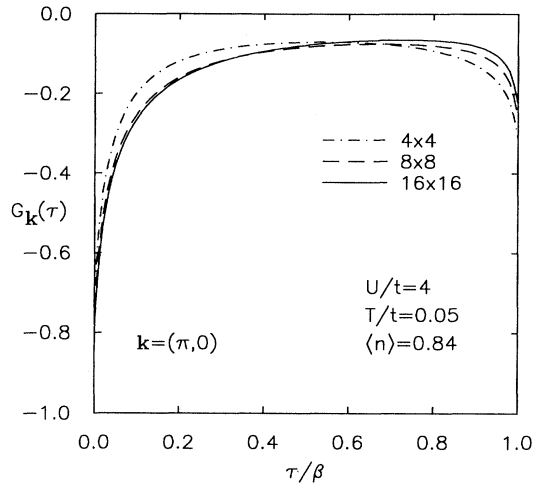

FIG. 12. Dependence of the FLEX Green's function on discretization scale at low temperature ($T/t=0.05$).

where Ω is the high-frequency cutoff ($\sim 40t$ in this case) and $G_{\mathbf{k}}^0$ is the noninteracting Green's function calculated with the chemical potential μ of the interacting system:

$$G_{\mathbf{k}}^0(i\omega_n)=\frac{T}{i\omega_n-(\epsilon_{\mathbf{k}}-\mu)} . \tag{3.2}$$

The extension of the frequency sum to infinity is necessary to prevent the appearance of oscillations with frequency Ω in the Fourier transform (see Sec. III B).

In general, results from the 8^2 and 16^2 discretizations differ negligibly for temperatures of order $T/t=0.1$ and higher. In most of the remaining figures in this paper an 8^2 discretization is employed. An exception is the plot of t-matrix eigenvalues in Sec. III D, for which a 16^2 discretization was employed to treat substantially lower temperatures.

Note that the effects of discretization in SCF solutions are quite different from finite-lattice effects in exact diagonalization and QMC studies. On finite lattices the effect of low-energy fluctuations is limited by the presence of a gap in the excitation spectrum. For this reason, long-range order exists at all temperatures in a periodically continued finite system; the presence or absence of long-range order in the corresponding infinite system can be determined using finite-size scaling. In contrast, SCF approximations are more likely to *underestimate* the degree of long-range order when solved on coarse **k**-space meshes. This is because the fluctuations corresponding to a single value of **Q** enter with *finite* weight in discrete Brillouin zone sums; the contribution of a singular mode diminishes as the fineness of the mesh is increased and the sum more closely approximates the underlying integral. In Fig. 14 we compare finite-mesh effects in FLEX and QMC calculations of the staggered susceptibility $\chi_q(\tau),\mathbf{q}=(\pi,\pi)$. The temperature and density are fixed at $T/t=0.25$ and $\langle n\rangle=0.875$. The FLEX calculations shown omit the Aslamazov-Larkin (AL) diagrams. The imaginary-time correlation functions are calculated as before:

$$\chi_{\mathbf{q}}(\tau)=T\sum_{\nu_m=-\Xi}^{\Xi} e^{-i\nu_m\tau}[\chi_{\mathbf{q}}(i\nu_m)-\chi_{\mathbf{q}}^0(i\nu_m)] +\chi_{\mathbf{q}}^0(\tau) , \tag{3.3}$$

with $\chi_{\mathbf{q}}^0$ the noninteracting susceptibility corresponding to the interacting chemical potential. The cutoff used in the Fourier transform of susceptibilities (in this case $\Xi\sim 10t$) is generally smaller than in the calculation of the single-particle Green's function [Eq. (3.1)].

Note that for both the 4^2 and 8^2 meshes the QMC result is larger than the FLEX, consistent with the argu-

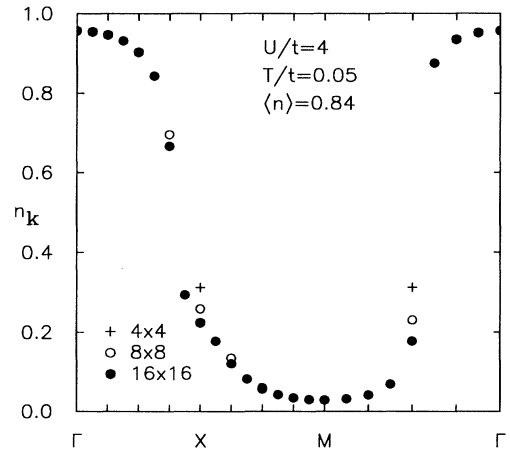

FIG. 13. Dependence of the FLEX occupancy factor on discretization scale at low temperature ($T/t=0.05$).

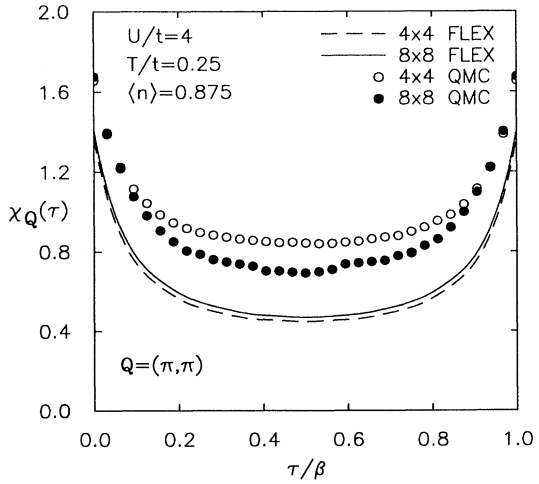

FIG. 14. Dependence of the FLEX magnetic correlation function $\chi_q(\tau)$ on discretization scale at intermediate temperature ($T/t=0.25$). For comparison, the finite-size dependence of the QMC correlation function is also shown. Note that the QMC result is markedly more size dependent and that the size dependence within the two calculation schemes is in opposite directions.

ments above. Note also that the QMC result is considerably more size dependent. The agreement between FLEX and QMC calculations for this property (which is particularly sensitive to finite-size effects) would be expected to improve further on finer meshes.

B. Finite frequency cutoff

When SCF equations are solved on the imaginary axis, an approximate discretization of the energy variable is not necessary: the Matsubara frequencies naturally provide a discrete mesh. It is still necessary, however, to introduce a high-energy cutoff on frequency sums. In this section we discuss the quantitative effect of this cutoff on calculated properties.

We have generally used a constant cutoff Ω of $10t$ or $40t$ for calculations of single-particle properties. For example, the mean density takes the form

$$\langle n \rangle = 1 + 2 \sum_{\omega_n = -\Omega}^{\Omega} G_{\mathbf{k}}(i\omega_n) \ . \tag{3.4}$$

Sums of this type may be approximately extended to infinity by adding in contributions for $|\omega_n| > \Omega$ from the corresponding noninteracting system with the same chemical potential. We have generally avoided this procedure, except when computing Fourier transforms *after* the completion of a self-consistent calculation [see Eqs. (3.1) and (3.3)]. The reason is technical: when complete vertices of the form

$$(\mathbf{1} - \mathbf{VR})^{-1}\mathbf{V}$$

are computed, a large-scale matrix inverse is required. In the simplest case the complete vertex takes the form

$$\frac{U}{1 - U\bar{\chi}_{\mathbf{q}}(i\nu_m)} \ ,$$

with

$$\bar{\chi}_{\mathbf{q}}(i\nu_m) = -\frac{\beta}{N} \sum_{\mathbf{k}} \sum_{\omega_n = -\Omega}^{\Omega} G_{\mathbf{k}+\mathbf{q}}[i(\omega_n + \nu_m)] G_{\mathbf{k}}(i\omega_n) \ . \tag{3.5}$$

(When $\bar{\chi}$ is calculated in this manner, factors of G must be set to zero when their frequency labels fall outside the imposed cutoffs.) It is simple to extend the frequency sum in Eq. 3.5 to infinity using noninteracting Green's functions. The extension is not so simple, however, when a full matrix inverse must be performed. Since the instantaneous portion of the irreducible vertex allows arbitrarily large energy transfers in particle-hole and particle-particle scattering, a nonconsistent treatment of high-energy contributions may introduce large errors, particularly in nearly singular matrix inverses. For this reason we have chosen not to extend frequency sums to infinity within self-consistent calculations. The effect of temperature-independent high-frequency cutoffs may then be studied systematically.

The frequency extensions used in Fourier transforms have a different purpose. In this case low-frequency components, which have previously been calculated with an imposed cutoff, are unaffected by an extension. The extension serves only to eliminate high-frequency "ripple" in calculated Fourier transforms.

In Fig. 15 we compare results for the single-particle Green's function $G_{\mathbf{k}}(\tau)$, $\mathbf{k} = (\pi, 0)$, obtained using cutoffs $\Omega = 10t$ and $40t$ (2.5 and 10 times the half-width of the noninteracting 2D band). The temperature $T/t = 0.25$, and the mean density $\langle n \rangle = 0.84$. Comparisons for the staggered susceptibility $\chi_{\mathbf{q}}(\tau)$, $\mathbf{q} = (\pi, \pi)$, are shown in Fig. 16. In each case the cutoff for the final calculation of the vertex-corrected $\chi_{\mathbf{q}}(i\nu_m)$ is $|\nu_m| \leq \Xi = \Omega/4$. The dependence on the cutoff is considerably stronger for the susceptibility than for the Green's function. (In fact, the large-**Q** magnetic susceptibility, which involves a nearly singular vertex correction, exhibits the most cutoff dependence of any correlation function.) In most of the remaining figures in this paper the cutoff Ω is set at $40t$.

C. Contribution of Aslamazov-Larkin diagrams

In general two sorts of contributions to the irreducible vertex V for particle-hole and particle-particle scattering emerge from functional differention[11,17,18] of the FLEX self-energy: (a) exchange of a single RPA-like fluctuation and (b) conversion of the initial-state pair to two distinct RPA-like fluctuations and subsequent recombination in the final state. We shall call the second set of contributions Aslamazov-Larkin (AL) diagrams by analogy with the corresponding terms in the fluctuation conductivity of superconductors.

The AL diagrams are expensive to calculate in comparison with the one-fluctuation–exchange diagrams, since they require an additional sum on internal frequency and momentum. They must, however, be included to make calculations of the two-particle Green's function rigorously conserving. As an example, their effect can be demonstrated by calculating the uniform susceptibility for magnetic and density excitations, $\chi_m(\mathbf{Q}=0, i\nu_m)$ and

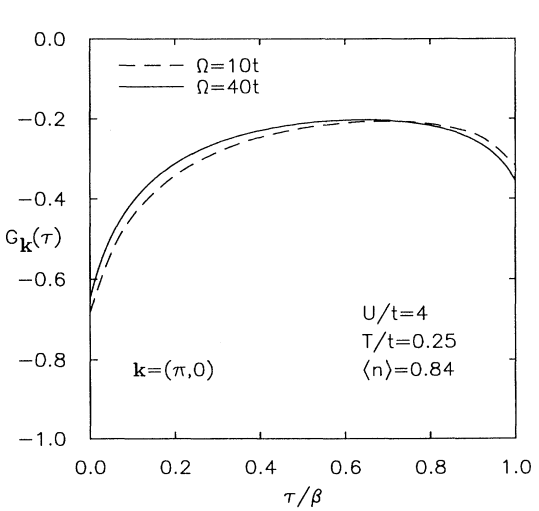

FIG. 15. Dependence of the FLEX Green's function $G_{\mathbf{k}}(\tau)$ on frequency cutoff Ω. Finite cutoff corrections are relatively insensitive to temperature for $T/t < 0.5$.

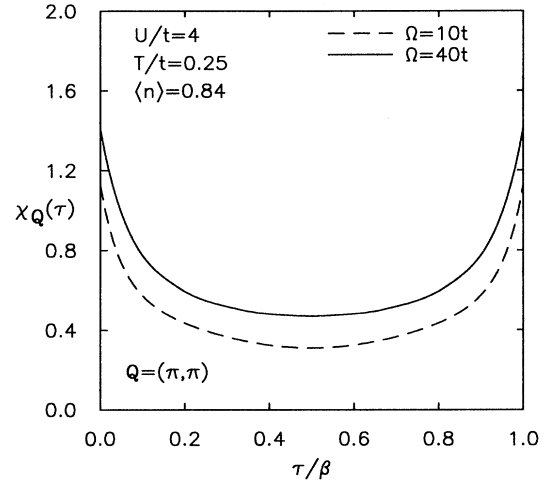

FIG. 16. Dependence of the FLEX magnetic correlation function $\chi_q(\tau)$ on frequency cutoff Ω. Results are shown for $\mathbf{q}=(\pi,\pi)$ at intermediate temperature.

$\chi_d(\mathbf{Q}=0,i\nu_m)$. Since the total spin and particle number of the system are globally conserved, both susceptibilities vanish for $\nu_m\neq 0$ when computed exactly. The finite-frequency components should also vanish exactly within any conserving approximation. For example, this condition is satisfied by Hartree-Fock (i.e., the RPA), since for $\mathbf{Q}=0$ and $\nu_m\neq 0$,

$$\chi_m^0(\mathbf{Q}=0,i\nu_m)=\chi_d^0(\mathbf{Q}=0,i\nu_m)$$
$$=-\frac{1}{N}\sum_{\mathbf{k}}\frac{f_{\mathbf{k}}-f_{\mathbf{k}+0}}{\epsilon_{\mathbf{k}}-\epsilon_{\mathbf{k}+0}-i\nu_m}=0\ . \qquad (3.6)$$

In Figs. 17 and 18 the uniform susceptibilities for

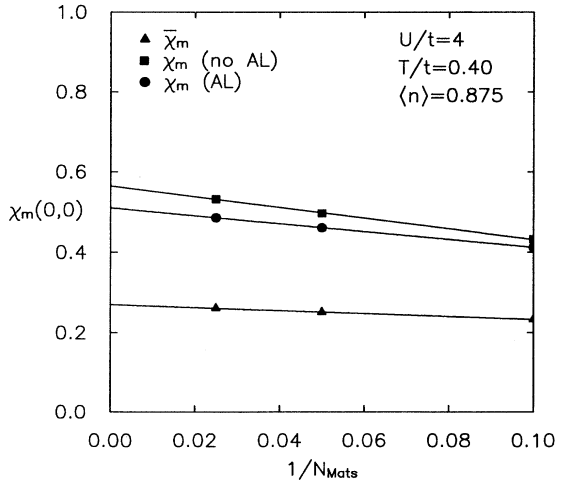

FIG. 17. Plot of the $\mathbf{q}=0$, $\nu_m=0$ magnetic susceptibility as a function of N_{Mats}^{-1}. Results are shown for $\bar{\chi}$ (which omits vertex corrections), and for the vertex-corrected χ with and without AL diagrams. Results for $N_{\text{Mats}}\to\infty$ follow by linear extrapolation.

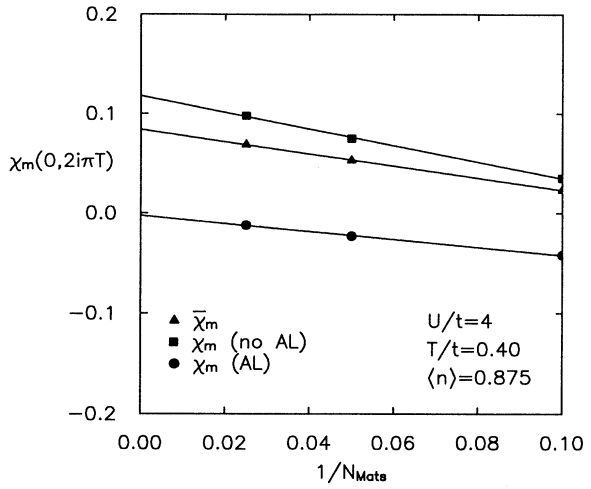

FIG. 18. Plot of the $\mathbf{q}=0$, $\nu_m=2\pi T$ magnetic susceptibility as a function of N_{Mats}^{-1}. Note that when AL diagrams are included, the susceptibility extrapolates to zero, as required by the conservation law on total spin. The quantitative violation of the conservation law remains small when AL diagrams are omitted.

$\nu_m=0$ and $\nu_m=2\pi T$ are plotted as a function of the number of Matsubara frequencies, N_{Mats}, retained in the calculation. [In general, we calculate with a fixed cutoff $\Omega=40t$ and do not extrapolate Ω (or N_{Mats}) to infinity. The value of $\chi_m(\mathbf{Q}=0,\ \nu_m=2\pi T)$ is so small that an extrapolation becomes necessary for fractional accuracy.] Results are shown for FLEX calculations with and without the AL correction. Even if the correction is omitted, the result for $\nu_m=2\pi T$ is smaller by roughly an order of magnitude than the result for $\nu_m=0$. It is clear that the finite-frequency result (Fig. 18) which includes the correction extrapolates to zero, while the result which omits the correction does not; the quantitative violation of the conservation law is, in any case, small. Furthermore, the AL correction to the zero-frequency susceptibility is of order 10%.

In more detailed comparisons of zero-frequency susceptibilities with and without AL diagrams the size of the correlation remains of order 10–15 %. The effect on the staggered susceptibility is illustrated in Fig. 19. In this case and several others the AL diagrams cause the agreement with finite-lattice QMC calculations to deteriorate, rather than to improve. This is perhaps intuitively unexpected; however, the source of this effect is closely related to the improvements which result when the FLEX approximation is replaced by a higher iteration of the parquet solution. For the density shown in Fig. 19 the AL correction to the irreducible magnetic vertex weakens the attraction between a particle-hole pair, reducing the susceptibility. This same weakening should be felt in the magnetic fluctuation contribution to the self-energy: a weaker attraction again implies a reduced effect. Roughly speaking, this should lead to an increased effective density of states and susceptibility. The AL diagrams reduce the agreement with QMC since they lead to an asymmetric treatment of the particle-hole vertex and the single-particle self-energy. This treatment is necessary,

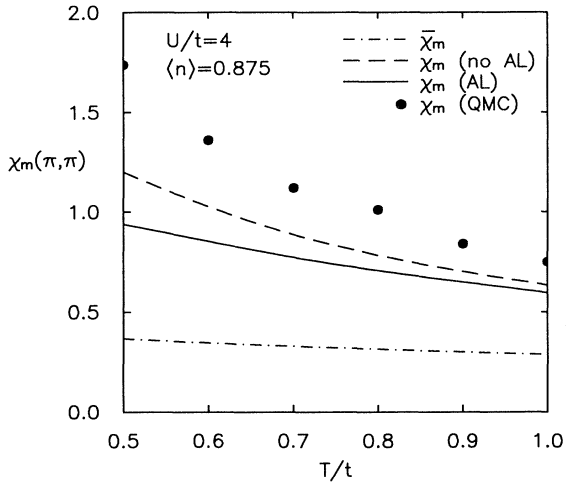

FIG. 19. Temperature dependence of the zero-frequency staggered magnetic susceptibility from FLEX and QMC. Note that one-fluctation-exchange vertex corrections substantially increase χ_m over $\bar{\chi}_m$; in contrast, the AL diagrams reduce χ_m and worsen the agreement with QMC.

however, in a rigorously conserving approximation.

In an iterative solution of the parquet equations (see Sec. II), the AL diagrams appear first at the next level beyond the appearance of the one-fluctuation-exchange diagrams. At this level the AL diagrams serve as the "two-rung" contributions to full ladders based not on the bare vertices, but on the compound vertices introduced in I. Compound vertices also appear on fluctuation propagators in the self-energy at this level, partially offsetting the AL contributions as remarked earlier.

In detailed calculations two treatments of the AL diagrams are possible: (a) if it is essential to satisfy conservation laws exactly within numerical accuracy, the diagrams must be retained. This might be the case, for example, in low-frequency transport calculations. (b) In a systematic iterative solution of the parquet equations the diagrams should be omitted. We shall adopt the second point of view throughout the remainder of this paper. In this light the parquet approach is considered fundamental; the partial quantitative success of the FLEX approximation derives from its being a step in the iterative solution of the full parquet.

D. *T*-matrix eigenvalues

As discussed in Sec. IV B of I, SCF techniques may be used to search for normal-state instabilities which signal second-order phase transitions. We have previously published an approximate phase diagram[25,26] for the partially filled Hubbard model, obtained using the FLEX approximation (without AL diagrams). In this section we briefly review our earlier work and comment on the changes which result from (a) the inclusion of the AL diagrams and (b) the extension to a parquet approximation.

For a coarse Brillouin zone and intermediate temperatures the eigenvalue problem

$$(-\beta V\bar{R})\phi=\lambda\phi \tag{3.7}$$

may be solved by exact diagonalization using a standard routine. In the nearly half-filled Hubbard model the largest eigenvalue at high temperatures occurs in a magnetic channel with total momentum $\mathbf{Q}$ near (π,π). The exact momentum (subject to the discretization scale) is dependent on both filling and temperature. As the temperature is lowered, a competing eigenvalue appears in the singlet particle-particle channel with discrete d-wave rotational symmetry. This d-wave eigenvalue rapidly dominates all other particle-particle eigenvalues.

At lower temperatures the evolution of the leading eigenvalues in the magnetic and d-wave singlet channels may be followed using the projection technique described in Sec. IV B of I. The behavior of the eigenvalues for various fillings based on a 16^2 Brillouin zone discretization is shown in Figs. 20 and 21. In some cases magnetic eigenvalues are shown for multiple values of $\mathbf{Q}$, in order to trace out the motion of the maximum away from (π,π) as the temperature is decreased. Several points should be noted: first of all, for the fillings $\langle n\rangle=1$ and 0.96 the $\mathbf{Q}=(\pi,\pi)$ magnetic eigenvalue reaches unity, signaling a magnetic ordering "transition." This transition has mean-field character, as in Hartree-Fock theory, and should be interpreted as a crossover to a region with an exponentially large correlation length. Further from half-filling the magnetic eigenvalues saturate or slowly decrease, and the d-wave eigenvalue eventually reaches unity instead. Again the approximation leads to a transition with mean-field character, rather than the Kosterlitz-Thouless behavior which must be present in two dimensions.

The resulting phase diagram (Fig. 22) indicates the qualitative nature of the normal-state–ordered-state

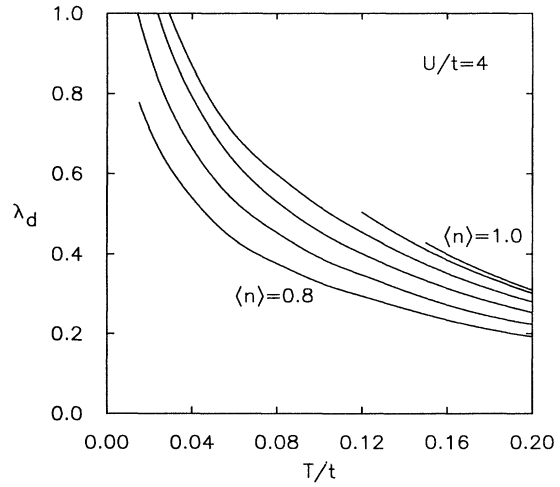

FIG. 20. Maximum t-matrix eigenvalue for d-wave singlet particle-particle scattering, λ_d. A 16^2 Brillouin zone discretization is employed. Results are shown for six densities varying from $\langle n\rangle=1.0$ to 0.8 by increments of 0.04. An eigenvalue of unity signals a (mean-field-like) transition to a superconducting state.

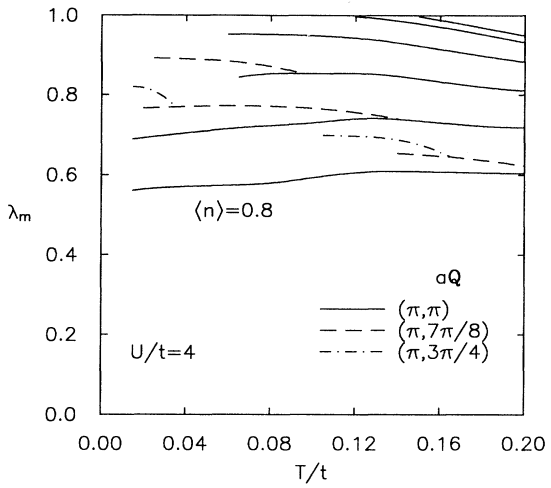

FIG. 21. Maximum t-matrix eigenvalue for magnetic particle-hole scattering with total momentum $\mathbf{Q}$, $\lambda_m(\mathbf{Q})$. Results are shown for the same six densities used in Fig. 20. For densities below $\langle n \rangle = 1.0$, the maximum eigenvalue moves away from $\mathbf{Q}=(\pi,\pi)$ at low temperatures. One or more incommensurate eigenvalues are shown for $\langle n \rangle = 0.88$, 0.84, and 0.80. For clarity these eigenvalues are only plotted in a limited range of temperatures.

phase boundary. It suggests the presence of a region of superconductivity mediated by the antiferromagnetic spin fluctuations, but does not rigorously establish the existence of such a phase. Furthermore, the phase diagram has nothing to say about the nature of the *ground state* away from half-filling; calculations in both the weak- and strong-coupling limits suggest the ground state remains magnetic near $\langle n \rangle = 1$, but becomes incommensurate ($\mathbf{Q} \neq (\pi,\pi)$). Within mean-field theories this implies the existence of a first-order boundary separating a low-temperature incommensurate phase from a high-temperature commensurate phase.

The exact shape of the magnetic-superconducting boundary in Fig. 22 is not well determined. It seems likely, however, that a magnetic state with finite T_N gives way directly to a superconducting state with finite T_c.

Figures 20–22 are results from the FLEX approximation without AL diagrams. As argued in the last section, susceptibilities become less accurate when these diagrams are included; presumably the same effect occurs for t-matrix eigenvalues. In particular, the AL corrections lead to a decrease of order 10% in magnetic eigenvalues (see Fig. 23). This is enough to destroy the finite-temperature magnetic phase transition found in Fig. 21. The physical basis for this destruction of long-range order is incorrect, however. As before, we would prefer to view the AL diagrams as contributions to the next level of the iterative parquet solution.

As a next step, it is natural to ask the fate of the t-matrix eigenvalues within the full parquet solution. Since the same irreducible vertices appear in the complete two-particle vertex Γ and in the self-energy Σ, the appearance of a finite-temperature pole in Γ would necessarily be accompanied by a divergent fluctuation contribution to Σ: assuming the pertinent zero-frequency fluctuation propagator varies as $1/q^2$, with $\mathbf{q}$ the deviation from the ordering vector $\mathbf{Q}$, the contribution to the self-energy diverges as

$$\int_{\Lambda} \frac{d\mathbf{q}}{q^2} \sim \ln\Lambda \ . \tag{3.8}$$

Such a divergence cannot occur, however, within a self-consistent solution. For this reason, subject to the as-

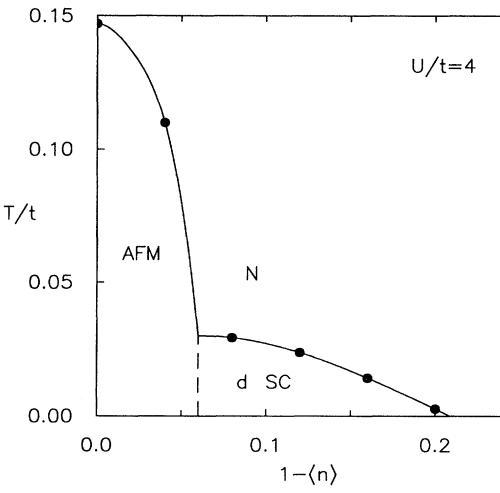

FIG. 22. Phase diagram for the partially filled Hubbard model, determined from the eigenvalues in Figs. 20 and 21. Only the boundary between the normal and ordered states is calculated: additional transitions (e.g., a first-order transition from a commensurate to incommensurate antiferromagnetic state) may occur at lower temperatures. The dashed line separating the antiferromagnetic and superconducting states is only a guide to the eye. All transitions are to be interpreted in a mean-field sense, as discussed in the text. Note finally that the d-wave transition temperature at $1-\langle n \rangle = 0.2$ has been extrapolated from Fig. 20.

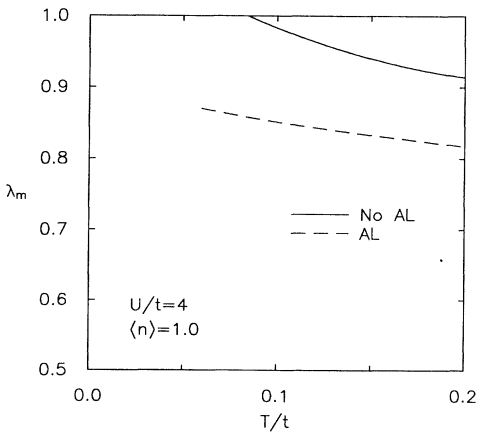

FIG. 23. Effect of AL diagrams on the commensurate magnetic eigenvalue $\lambda_m(\mathbf{Q})$, $\mathbf{Q}=(\pi,\pi)$. A 4^2 Brillouin zone discretization is employed for this calculation only. The mean density is $\langle n \rangle = 1.0$. The AL diagrams weaken the vertex sufficiently to destroy the instability altogether.

sumed form for the fluctuation propagator, the full parquet equations suppress any phase transition in one or two dimensions to zero temperature. In one dimension the parquet approach is known to yield the correct zero-temperature critical behavior of susceptibilities when logarithmic singularities are summed using the renormalization-group formalism.

Since the parquet approach prevents finite-temperature instabilities in low dimensions, we have not applied the pseudopotential approximation of Sec. II to study the t-matrix eigenvalues.[27] Instead we view the phase diagram obtained within the FLEX approximation as indicative of a *tendency* toward anisotropic pairing at low temperatures. More definitive statements may require the exact solution of the parquet equations (without the pseudopotential approximation).

E. One-particle correlation functions

In the remainder of this paper we concentrate on calculating correlation functions for comparison with QMC. While finite-discretization effects in SCF calculations are not equivalent to finite-lattice effects in QMC, such comparisons should be valid when both effects are small. We begin by comparing results for the single-particle Green's function $G_{\mathbf{k}}(\tau)$ and $\mathbf{k}$-space occupancy factor $n_{\mathbf{k}}$.

The imaginary-time Green's function $G_{\mathbf{k}}(\tau)$ may be compared directly with QMC results to evaluate the accuracy of an approximation. Since the SCF calculations yield imaginary-frequency functions, Fourier transforms must be performed using the method of Eq. (3.1). (The QMC simulations are performed in real space and imaginary time, so finite Fourier transforms to $\mathbf{k}$ space have been performed to obtain the QMC data shown below.)

The temperature dependence of the three pseudopotentials U_m, U_d, and U_s for the parquet calculations are shown in Figs. 24 and 25. Results are shown for a 4^2 discretization with densities $\langle n \rangle = 1.0$ and 0.875. In all cases $U/t = 4$. For half-filling the density and singlet pseudopotentials are identical. This is a consequence of the pseudopotential definitions and particle-hole symmetry: U_d is defined in terms of $\chi_d(\mathbf{Q}, i\nu_m = 0)$ with $\mathbf{Q} = (\pi, \pi)$, while U_s is defined in terms of $\chi_s(\mathbf{0}, i\nu_m = 0)$; at half-filling

$$\chi_d(\mathbf{Q},0) = \chi_s(\mathbf{0},0) \ . \tag{3.9}$$

Several points should be noted about the behavior of the pseudopotentials. First of all, fluctuations in crossed channels increase the repulsion in the density and singlet channels and decrease the attraction in the magnetic channel. The latter effect is quantitatively most important, since only the magnetic channel becomes singular. All three pseudopotentials are weakly temperature-dependent, as anticipated from the qualitative Berk-Schrieffer arguments of Sec. II. Finally, the potentials are almost independent of the discretization scale: this is important calculationally, since results from the coarse discretization may be used as the initial input for the fine-scale calculation.

In principle, the imaginary-time Green's function $G_{\mathbf{k}}(\tau)$ contains complete information on single-particle properties. For example, the occupancy factors $n_{\mathbf{k}}$ may be obtained directly as

$$n_{\mathbf{k}} = -\lim_{\tau \to \beta^-} G_{\mathbf{k}}(\tau) = 1 + \lim_{\tau \to 0^+} G_{\mathbf{k}}(\tau) \ . \tag{3.10}$$

The Green's function may be decomposed formally as

$$G_{\mathbf{k}}(\tau) = -\frac{1}{Z} \sum_{nm} e^{-\beta E_n} e^{-\tau(E_m - E_n)} |\langle m | c_{\mathbf{k}}^{\dagger} | n \rangle|^2 \ , \tag{3.11}$$

where $|n\rangle$ and $|m\rangle$ are eigenstates of $H - \mu N$. In numerical calculations it is generally difficult to obtain detailed information on high-energy excitations (large $E_m - E_n$), since these contributions to $G_{\mathbf{k}}(\tau)$ die rapidly away from

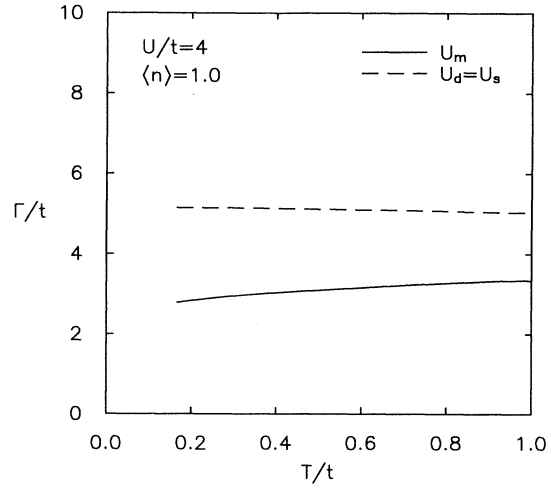

FIG. 24. Temperature dependence of the parquet pseudopotentials U_m, U_d, and U_s for $\langle n \rangle = 1.0$. Note that the attractive magnetic vertex is weakened in magnitude, while the other two repulsive vertices are enhanced. Within our calculational scheme (see Sec. II B), the density and singlet pseudopotentials are identical at $\langle n \rangle = 1.0$. Results from 4^2 and 8^2 discretizations are the same within 2%.

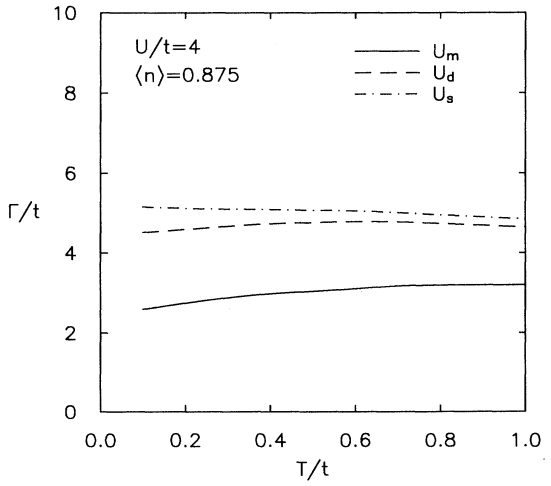

FIG. 25. Temperature dependence of the parquet pseudopotentials U_m, U_d, and U_s for $\langle n \rangle = 0.875$. As in Fig. 24, results from 4^2 and 8^2 discretizations are the same within 2%.

$\tau=0$ and $\tau=\beta$.

In Figs. 26 and 27 we compare results for the Green's function from SCF and QMC calculations for two parameter choices. Results are shown for half-filling (Fig. 26) and $\langle n \rangle = 0.875$ (Fig. 27). For $\langle n \rangle = 0.875$, the FLEX approximation captures the qualitative trend in functional forms, while the parquet approximation is quantitatively accurate. On the other hand, neither approximation is accurate at low temperatures for $\langle n \rangle = 1.0$. The deviations at half-filling may be due to a number of sources. First of all, it is possible the disagreement signals a breakdown of the parquet approach: presumably, a single-particle gap Δ exists at zero temperature for all values of U when $\langle n \rangle = 1$ (as in one dimension). The behavior of the parquet equations for temperatures $T < \Delta$ is then uncertain; even if the parquet approach remains robust, errors introduced by our pseudopotential approximation may be unacceptable in this case. As a second possibility, if the temperature in Fig. 26 is actually *larger* than the zero-temperature gap, the disagreement may be due to the contrasting finite-size behavior of the parquet and QMC solutions. At sufficiently low temperatures, the finite lattices studied by QMC always have ordered spins and a well-defined single-particle gap. In contrast, the parquet solution (even when obtained using a discretized Brillouin zone) corresponds to an infinite system with a finite magnetic correlation length and no single-particle gap. At a specified temperature the two approaches should disagree if the QMC lattice size is smaller than the correlation length.

Away from half-filling, the parquet calculation of $G_{\mathbf{k}}$ remains accurate for all values of T studied here. Nevertheless, our results do not rule out a breakdown of the parquet solution at significantly lower temperatures. Furthermore, the pseudopotential approximation may at some point fail while the exact solution remains valid. The strongest argument for the continued validity of the full parquet equations at lower temperatures is their successful use in the analysis of singular contributions to correlation functions in one dimension.

For completeness, in Figs. 28 and 29 we compare calculations of the occupancy factor $n_{\mathbf{k}}$ along a contour in the Brillouin zone. As before, results are shown for $\langle n \rangle = 1.0$ and 0.875.

F. Susceptibilities

In this section we compare results for particle-particle and particle-hole susceptibilities. Our imaginary-axis technique yields zero-frequency ($i\nu_m = \nu = 0$) susceptibilities directly; in principle, this is enough to allow a search for second-order phase transitions. On the other hand, more detailed real-frequency information can only be obtained by analytic continuation from the imaginary axis. Progress in this area is discussed in Sec. III G. As before, comparisons with QMC results can still be made directly in imaginary frequency or time.

We begin with comparisons for various singlet-pair susceptibilities. Evidence from a number of sources suggests the partially filled Hubbard model has a tendency toward d-wave pairing. T-matrix eigenvalue studies (see

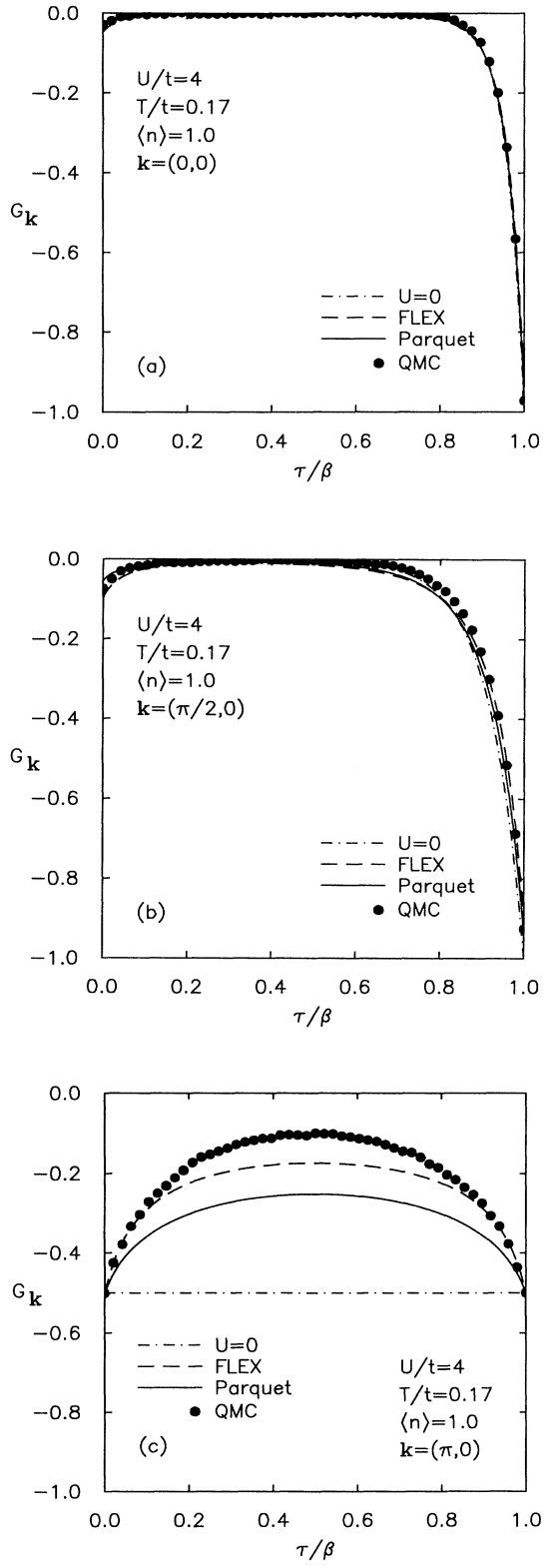

FIG. 26. Comparison of FLEX, parquet, and QMC Green's functions $G_{\mathbf{k}}$ for half-filling at $T/t = 0.17$. All results are for an 8^2 mesh. The $U=0$ Green's functions are shown to set the scale for correlation effects. (a) $\mathbf{k}=(0,0)$, (b) $\mathbf{k}=(\pi/2,0)$, (c) $\mathbf{k}=(\pi,0)$.

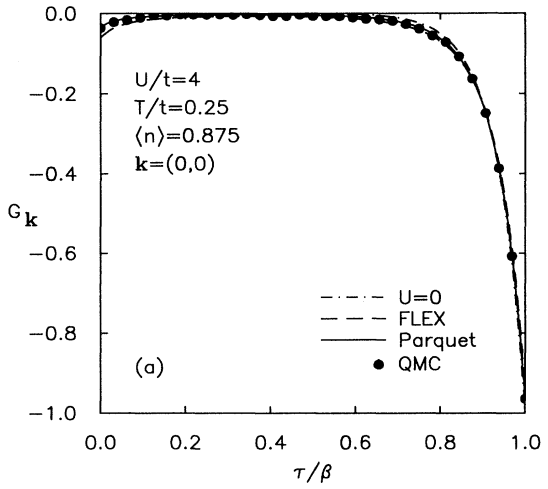

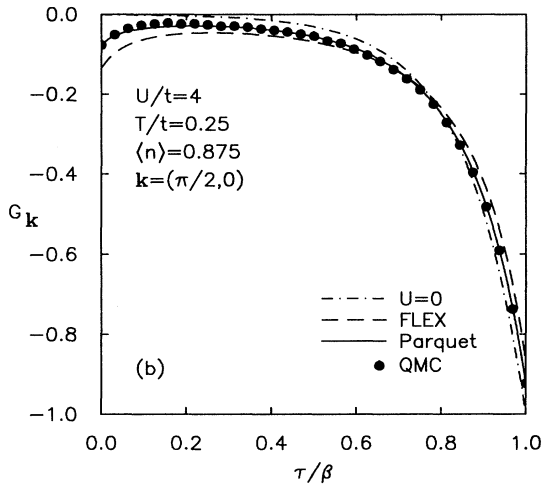

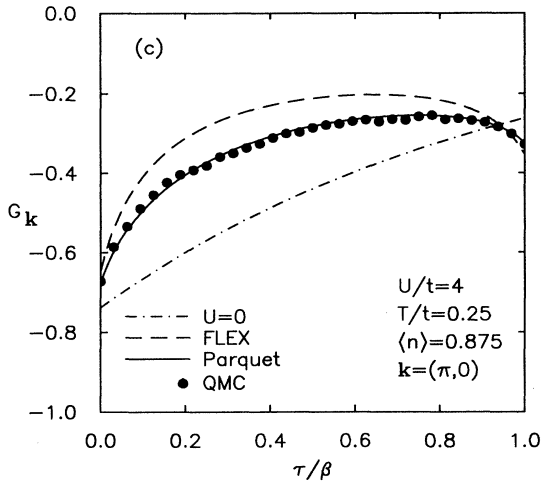

FIG. 27. Comparison of FLEX, parquet, and QMC Green's functions $G_{\mathbf{k}}$ for $\langle n \rangle = 0.875$ at $T/t = 0.25$. All results are for an 8^2 mesh. (a) $\mathbf{k} = (0,0)$, (b) $\mathbf{k} = (\pi/2,0)$, (c) $\mathbf{k} = (\pi,0)$.

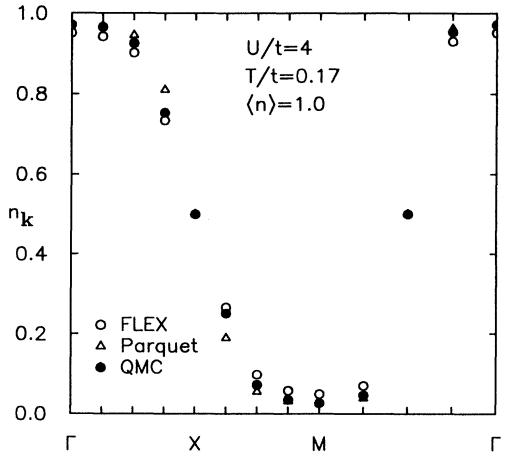

FIG. 28. Comparison of FLEX, parquet, and QMC occupancy factors $n_{\mathbf{k}}$ for half-filling at $T/t = 0.17$. All results are for an 8^2 mesh. The occupancy factor is plotted along the Brillouin zone contour $\Gamma \rightarrow X \rightarrow M \rightarrow \Gamma$.

Sec. III D) provide the most detailed picture of pairing strengths; static susceptibilities based on instantaneous pair-creation operators provide less detailed information, but are more readily calculable by QMC techniques. Such a susceptibility takes the form

$$\chi_g = \int_0^\beta d\tau \langle \Delta_g(\tau) \Delta_g^\dagger(0) \rangle \ , \tag{3.12}$$

where

$$\Delta_g^\dagger = \frac{1}{\sqrt{N}} \sum_{\mathbf{k}} g(\mathbf{k}) c_{\mathbf{k}\uparrow}^\dagger c_{-\mathbf{k}\downarrow}^\dagger \ . \tag{3.13}$$

Note $\Delta_g^\dagger$ creates a singlet (triplet) state for a function $g(\mathbf{k})$ with even (odd) parity. The state $\Delta_g^\dagger |\Omega\rangle$, with $|\Omega\rangle$ the empty band, is normalized to unity provided

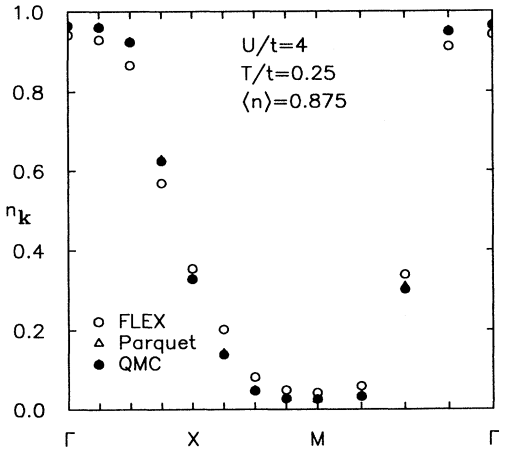

FIG. 29. Comparison of FLEX, parquet, and QMC occupancy factors $n_{\mathbf{k}}$ for $\langle n \rangle = 0.875$ at $T/t = 0.25$. All results are for an 8^2 mesh. Note that the parquet and QMC results agree within calculational accuracy along the entire contour.

$$\frac{1}{N}\sum_{\mathbf{k}}|g(\mathbf{k})|^2=1\ . \tag{3.14}$$

The real-space wave functions corresponding to various choices of g are summarized in Table I. Note that while the states $\Delta_g^\dagger|\Omega\rangle$ are orthonormal, the states $\Delta_g^\dagger|0\rangle$, with $|0\rangle$ the many-electron ground state, are not. For this reason, states belonging to the same representation of the rotation group are mixed by the action of the t matrix and do not correspond to independent scattering channels. (As an aside, this implies that sufficiently near an s-wave instability the susceptibilities corresponding to all three s-wave pair-creation operators should diverge.) The states belonging to different representations (s and d, for example) do not mix at any level. Note also that the wave functions $\Delta_g^\dagger|0\rangle$ correspond to instantaneous pairing; exact t-matrix eigenstates are strongly dependent on relative time (or frequency) due to the presence of the background Fermi sea. This means that the susceptibilities specified by Eq. (3.14) are not optimal for detecting instabilities.

FLEX and parquet results are compared with QMC simulations in Figs. 30 and 31. All results are for a 4^2 Brillouin zone, and the fillings are $\langle n\rangle=1.0$ and 0.875. Note first that the susceptibilities are in most cases markedly reduced from their values for $U=0$. This is the expected effect of the single-particle self-energy, discussed at greater length below. The FLEX approximation for $\langle n\rangle=0.875$ generally leads to an overcorrection, for the reasons mentioned in Sec. II A: the magnetic fluctuation propagator in Σ is too singular, since it contains the bare matrix element $-U$, rather than the weaker vertex Γ_m. In contrast, the pseudopotential parquet results are almost quantitatively accurate away from half-filling. As in Fig. 26, agreement with QMC is not exceptional at half-filling. The previous comments on gap formation at half-filling (Sec. III E) hold here as well.

Since the temperature range in Figs. 30 and 31 is too high to see direct signs of superconductivity (the max-

TABLE I. Real-space wave functions for simple choices of $g(\mathbf{k})$. Note that NN stands for nearest neighbor and NNN for next-nearest neighbor.

$g(\mathbf{k})$	Real space
1	On-site s
$\cos k_x+\cos k_y$	NN $s(s^*)$
$\cos(k_x+k_y)+\cos(k_x-k_y)$	NNN $s(s_{xy})$
$\cos k_x-\cos k_y$	NN $d(d_{x^2-y^2})$
$\cos(k_x+k_y)-\cos(k_x-k_y)$	NNN $d(d_{xy})$
$\sqrt{2}\sin k_x$	NN p
$\sqrt{2}\sin(k_x+k_y)$	NNN $p(p_{xy})$

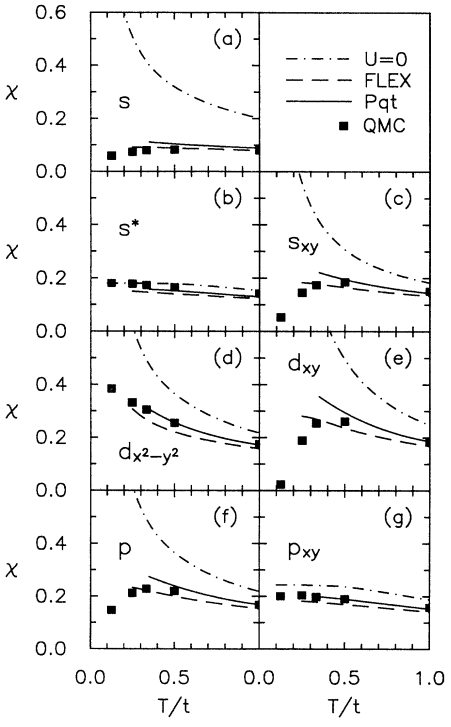

FIG. 30. Comparison of FLEX, parquet, and QMC results for seven particle-particle susceptibilities at $\langle n\rangle=1.0$. All results are for a 4^2 mesh. The choices for the pair wave function are (a) s, (b) s^*, (c) s_{xy}, (d) $d_{x^2-y^2}$, (e) d_{xy}, (f) p, and (g) p_{xy}. The unexceptional agreement between the SCF and QMC results at low temperature may be associated with magnetic gap formation in the 4^2 QMC lattice (compare Fig. 26).

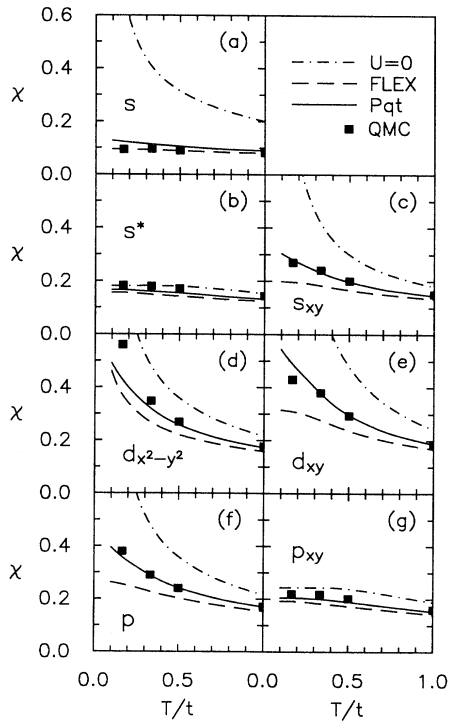

FIG. 31. Comparison of FLEX, parquet, and QMC results for seven particle-particle susceptibilities at $\langle n\rangle=0.875$. All results are for a 4^2 mesh. The pair wave functions are (a) s, (b) s^*, (c) s_{xy}, (d) $d_{x^2-y^2}$, (e) d_{xy}, (f) p, and (g) p_{xy}. The parquet results are in nearly quantitative agreement with QMC over a wide temperature range.

imum estimate for T_c in Sec. III D is only $T_c/t=0.03$), a more indirect approach is necessary. It is possible to separate the effect of single-particle renormalization from the enhancement (or suppression) caused by the two-particle vertex: formally, the susceptibility may be written

$$\chi_g=\bar{\chi}_g+\Delta\chi_g\ , \tag{3.15}$$

where $\Delta\chi_g$ contains the ladder sum based on the irreducible vertex (see Fig. 8). The contribution $\bar{\chi}_g$ is a physically unmeasurable quasiparticle density of states, which takes the place of the bare density of states in the strongly correlated system. Due mainly to the effect of low-frequency magnetic fluctuations,

$$\bar{\chi}_g \ll \chi_g^0 \tag{3.16}$$

for all the wave functions in Table I. This single-particle renormalization is responsible for the large suppression of the full susceptibilities shown in Figs. 30 and 31.

In order to have a superconducting instability the irreducible vertex must counteract the self-energy. The crossover in opposing effects need only occur at a temperature marginally higher than T_c itself. Nevertheless, potentially unstable channels can be identified at high temperatures as those with strongly temperature-dependent, positive values of $\Delta\chi_g$. Plots of $\Delta\chi_g$ for the previous parameter choices are shown in Figs. 32 and 33. The s^* and p_{xy} (next-nearest-neighbor p) enhancements are weakly positive, but nearly temperature independent. On the other hand, as expected from the earlier eigenvalue analysis, the $d_{x^2-y^2}$ enhancement grows rapidly with decreasing temperature. Note that FLEX and parquet results for $\Delta\chi_g$ are nearly the same. This is expected for the following reason: $\Delta\chi_g$ roughly measures the product of a vertex and an effective density of states. Within the parquet scheme, corrections which strengthen an attractive vertex tend to diminish the effective density of states. The product of the two is only weakly affected.

Next we consider calculations of the wave-vector-dependent magnetic susceptibility χ_Q. (The density, or charge, susceptibility may also be computed.) In Figs. 34 and 35, we show comparisons for the static susceptibility at several points in a 4^2 Brillouin zone. The parquet calculation is quite accurate away from half-filling, except for the $\mathbf{Q}=(\pi,\pi)$ component. We believe the (π,π) susceptibility is particularly subject to finite-size effects, and that this largely accounts for the deviation. To support this argument we compare parquet and QMC results for 4^2 and 8^2 Brillouin zones in Fig. 36. The disagreement between the two approaches decreases by about 50% in the larger system.

The parquet approach is also in good agreement with QMC for the finite-frequency susceptibility $\chi_q(i\nu_m)$. To

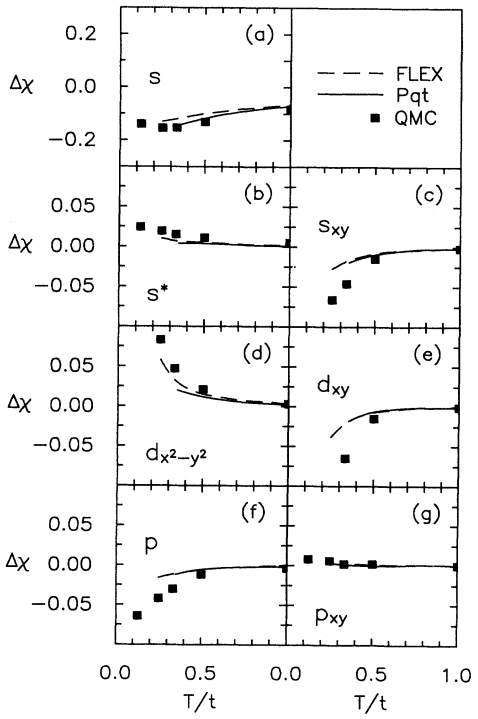

FIG. 32. Comparison of FLEX, parquet, and QMC results for the vertex correction $\Delta\chi$ in the particle-particle susceptibilities. As in Fig. 30, the density is $\langle n\rangle=1.0$, and a 4^2 mesh is employed in all calculations. The pair wave functions are (a) s, (b) s^*, (c) s_{xy}, (d) $d_{x^2-y^2}$, (e) d_{xy}, (f) p, and (g) p_{xy}. As in Figs. 26 and 30, agreement between SCF and QMC results at low temperatures is unexceptional.

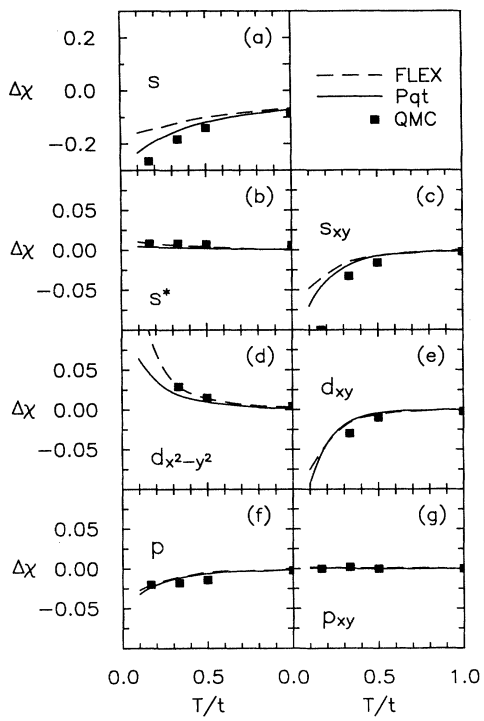

FIG. 33. Comparison of FLEX, parquet, and QMC results for the vertex correction $\Delta\chi$ in the particle-particle susceptibilities. As in Fig. 31, the density is $\langle n\rangle=0.875$, and a 4^2 mesh is employed in all calculations. The pair wave functions are (a) s, (b) s^*, (c) s_{xy}, (d) $d_{x^2-y^2}$, (e) d_{xy}, (f) p, and (g) p_{xy}. In this case both the FLEX and parquet results are in reasonable agreement with QMC (see discussion in the text).

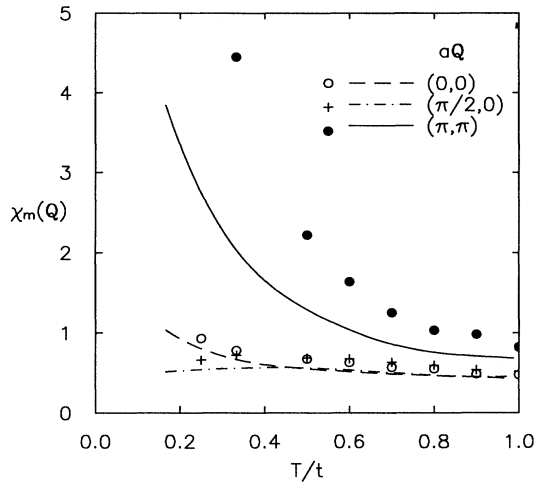

FIG. 34. Comparison of parquet and QMC results for the zero-frequency magnetic susceptibility $\chi_m(\mathbf{Q})$ as a function of temperature. The density is $\langle n \rangle = 1.0$, and a 4^2 discretization is employed. The Coulomb correlation is $U/t=4$. Parquet results are represented by lines, QMC results by symbols.

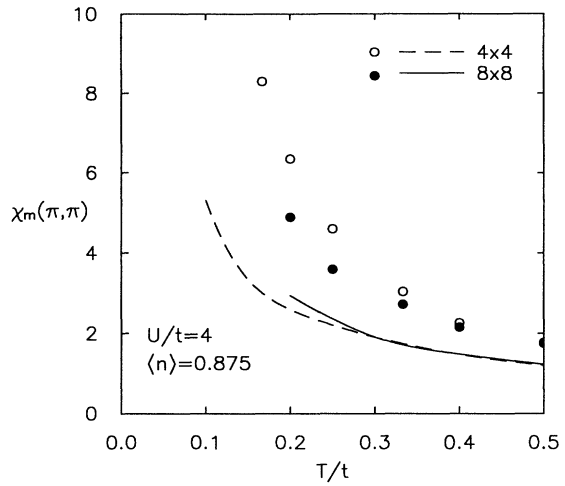

FIG. 36. Comparison of finite-mesh effects in parquet and QMC results for the zero-frequency staggered susceptibility, $\chi_m(\pi,\pi)$, at $\langle n \rangle = 0.875$. Note that the level of disagreement is reduced by roughly a factor of 2 by increasing the mesh scale from 4^2 to 8^2.

illustrate the comparison most clearly, we plot the property

$$\Delta\chi_{\mathbf{q}}(\tau) \equiv \chi_{\mathbf{q}}(\tau) - T\chi_{\mathbf{q}}(i\nu_m = 0) \tag{3.17}$$

for three values of $\mathbf{q}$ in Fig. 37. [The parquet curves are calculated by Fourier transform using Eq. (3.3).] Note that for $\mathbf{q}=0$ $\Delta\chi$ should be identically zero by a global conservation law; small deviations appear in the parquet result since the approach is not rigorously conserving. Note also that the finite-frequency property $\Delta\chi$ is quite accurately reproduced for $\mathbf{q}=(\pi,\pi)$ despite the deviations in the zero-frequency result.

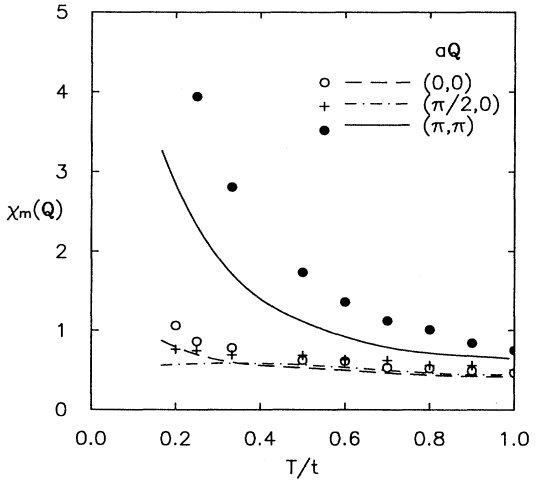

FIG. 35. Comparison of parquet and QMC results for the zero-frequency magnetic susceptibility $\chi_m(\mathbf{Q})$ as a function of temperature. The density is $\langle n \rangle = 0.875$, and other details are as in Fig. 34.

G. Real-frequency correlation functions

In order to recover information on real-frequency, or dynamic, correlation functions from the solution of imaginary-axis equations, it is necessary to perform a numerical analytic continuation. This process is subject to the same instabilities which accompany inverse Laplace transforms. The analytic continuation of QMC data is particularly difficult due to the presence of statistical noise. A number of techniques, some involving the use of model default functions, have recently been proposed to deal with this problem.[28–30]

The analytic continuation problem for SCF data is much better conditioned due to the absence of noise. In this case the Padé, or rational, approximant technique provides a viable solution. This method was first used in the present context by Vidberg and Serene.[31] The method consists of determining a rational function A/B which matches an imaginary-axis function at a set of Matsubara points, then using the approximant coefficients to extend the function to the entire complex plane. We have adapted the Vidberg-Serene algorithm to calculate the one-electron spectral density

$$\rho_{\mathbf{k}}(\omega) = -\frac{1}{\pi}\mathrm{Im}G_{\mathbf{k}}(\omega + i0^+) \tag{3.18}$$

and the magnetic spectral density

$$\sigma_{\mathbf{Q}}(\omega) = -\frac{1}{\pi}\mathrm{Im}\chi_{\mathbf{Q}}(\omega + i0^+) \; . \tag{3.19}$$

The reliability of the continuations depends on (a) the accuracy of the imaginary-axis calculation and (b) the number of points N_P used in fitting the approximant. The values of N_p required for our calculations are reasonably small, since the momentum-resolved spectral densities are relatively structureless.

Reliability checks are provided by sum rules:

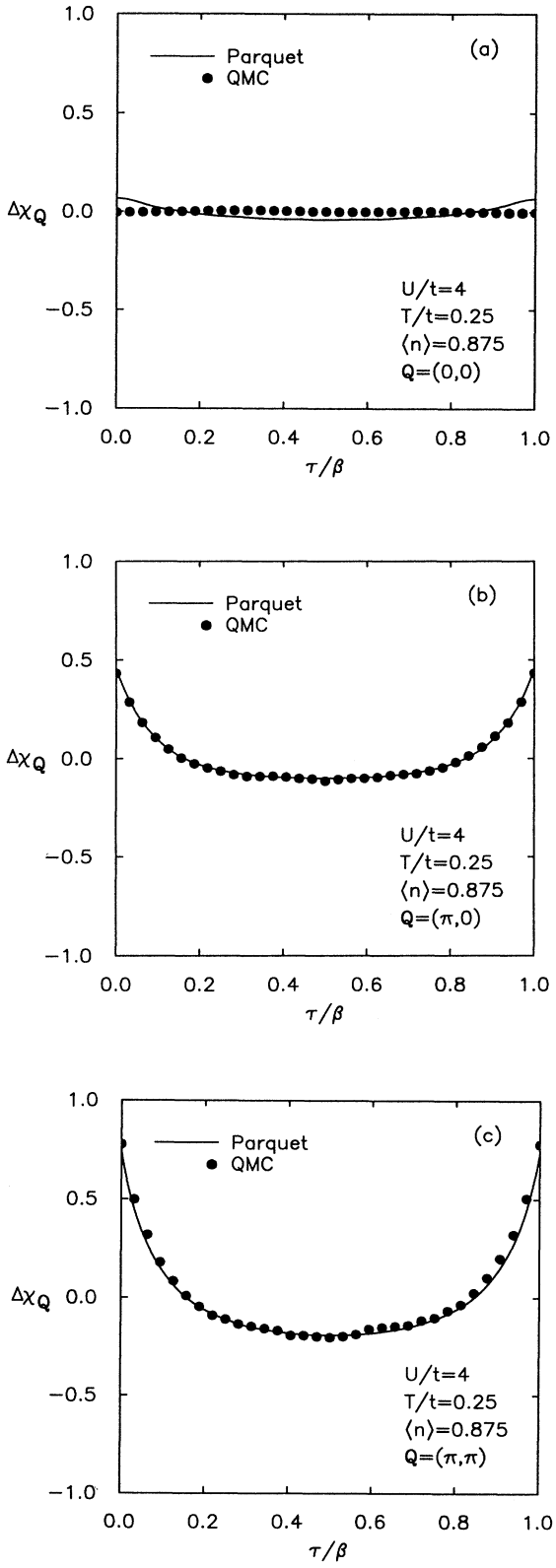

FIG. 37. Comparison of parquet and QMC results for the finite-frequency part of the magnetic correlation function, $\Delta\chi_{\mathbf{q}}(\tau)$. The density is $\langle n \rangle = 0.875$. (a) $\mathbf{q}=(0,0)$, (b) $\mathbf{q}=(\pi,0)$, (c) $\mathbf{q}=(\pi,\pi)$.

$$\int_{-\infty}^{\infty} d\omega \rho_{\mathbf{k}}(\omega) = 1 , \tag{3.20a}$$

$$\int_{-\infty}^{\infty} d\omega f(\omega)\rho_{\mathbf{k}}(\omega) = n_{\mathbf{k}} , \tag{3.20b}$$

$$\int_{-\infty}^{\infty} d\omega b(\omega)\sigma_{\mathbf{Q}}(\omega) = S_{\mathbf{Q}} , \tag{3.20c}$$

where $S_{\mathbf{Q}}$ is the magnetic structure factor $\langle m_z(\mathbf{Q}) m_z(-\mathbf{Q}) \rangle$; and f and b are the Fermi and Bose functions.[32] In numerical checks, we cut off the integrals at $\pm 10t$. Note that both $n_{\mathbf{k}}$ and $S_{\mathbf{Q}}$ are equal-time correlation functions which may be calculated directly as infinite Matsubara sums. Since data is available only at a finite set of points, we have extended both sums to infinity using the noninteracting correlation functions.[33]

Results for a representative set of spectral densities are shown in Figs. 38 and 39. The sum rules for these densities are satisfied at the 1% level. Note that the peaks in $\rho_{\mathbf{k}}$ for the noninteracting and interacting systems occur at

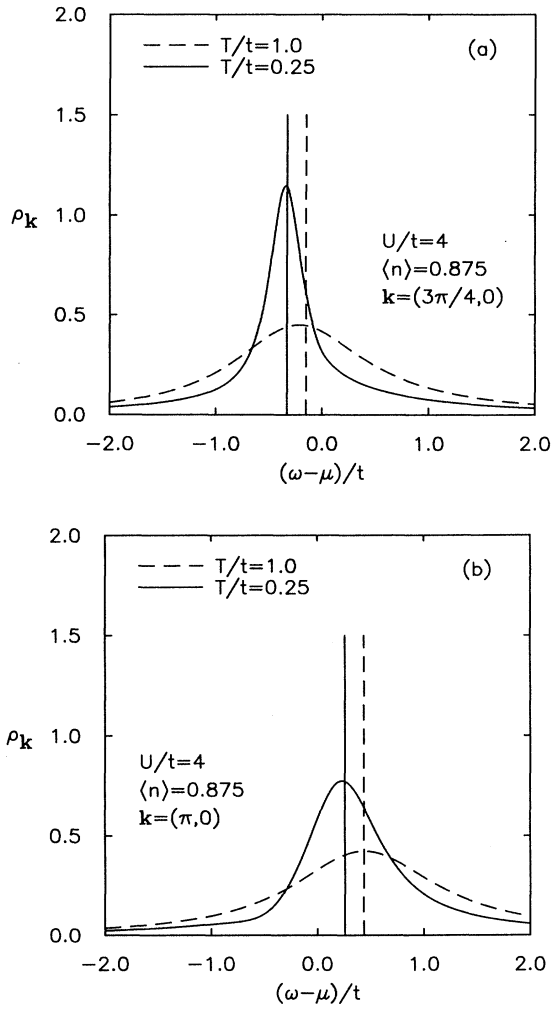

FIG. 38. Spectral density $\rho_{\mathbf{k}}$ from Padé continuation. An 8^2 discretization is employed. For each $\rho_{\mathbf{k}}$ shown, sum rules (3.20a)–(3.20b) are satisfied at the 1% level. Results are shown for $U/t=4$ and $U=0$ (δ functions). (a) $\mathbf{k}=(3\pi/4,0)$, (b) $\mathbf{k}=(\pi,0)$.

nearly the same values of $\omega-\mu$. This is expected since the total filling remains the same. The prominent inelastic peak in $\sigma_{\mathbf{Q}}$ for $\mathbf{Q}=(\pi,\pi)$ diminishes in calculations with a finer mesh.

Analytic continuation may also be used to study the detailed frequency dependence of the self-energy and conductivity. Both properties are subjects of great interest, but we defer their discussion for future work.

H. Equal-time correlations

Since QMC simulations are generally performed in real space and imaginary time, the simplest correlation functions to measure are on-site, equal-time properties. These include the magnetic moment

$$\langle m_z^2\rangle=\langle(n_\uparrow-n_\downarrow)^2\rangle\ , \tag{3.21}$$

the average double occupancy

$$\langle d\rangle=\langle n_\uparrow n_\downarrow\rangle=\tfrac{1}{2}[\langle n\rangle-\langle m_z^2\rangle]\ , \tag{3.22}$$

and the magnetic structure factor

$$S_{\mathbf{Q}}=\langle m_z(\mathbf{Q})m_z(-\mathbf{Q})\rangle\ ,$$
$$m_z(\mathbf{Q})=\frac{1}{\sqrt{N}}\sum_i e^{i\mathbf{Q}\cdot\mathbf{R}_i}m_z(\mathbf{R}_i)\ . \tag{3.23}$$

Such correlation functions are the most time consuming to calculate using methods based on imaginary frequency and momentum, since they require extensive summations. For example,

$$S_{\mathbf{Q}}=\langle T_\tau m_z(\mathbf{Q},\tau\to0)m_z(-\mathbf{Q},0)\rangle$$
$$=T\sum_m e^{-i\nu_m 0}\chi_{\mathbf{Q}}(i\nu_m)=T\sum_m\chi_{\mathbf{Q}}(i\nu_m)\ . \tag{3.24}$$

In turn

$$\langle m_z^2\rangle=\frac{1}{N}\sum_{\mathbf{Q}}S_{\mathbf{Q}}=\frac{T}{N}\sum_{\mathbf{Q},m}\chi_{\mathbf{Q}}(i\nu_m)\ . \tag{3.25}$$

The calculation of a single vertex-corrected component of $\chi_{\mathbf{Q}}(i\nu_m)$ is time consuming; the calculation of $\langle m_z^2\rangle$ for an N^2 discretization with L total Matsubara frequencies requires roughly $N^2L/16$ as much time (the factor of $\frac{1}{16}$ is gained by using symmetries efficiently). For this reason we have not studied equal-time correlation functions in great depth.[34]

In Figs. 40 and 41 we summarize results for the parquet approach for a 4^2 Brillouin zone with $\langle n\rangle=0.875$. The frequency sums which arise have been extended to infinity using noninteracting correlation functions. The agreement between parquet and QMC results is quite good for the local quantities $\langle m_z^2\rangle$ and $\langle d\rangle$: this is expected, since finite-size effects should be small for these properties. Note that for $U/t=4$ the double occupancy is reduced by approximately 50% and is almost temperature independent.

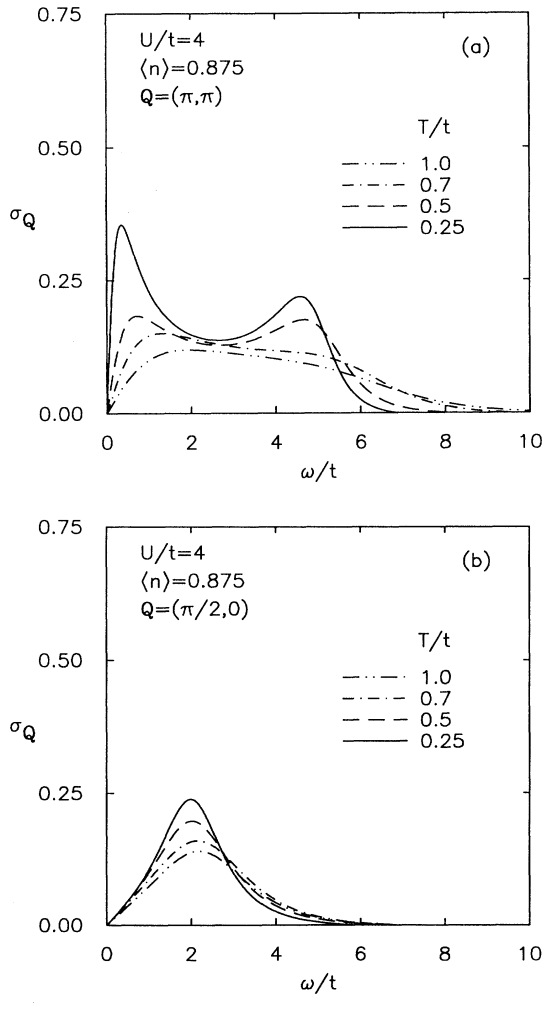

FIG. 39. Spectral density $\sigma_{\mathbf{Q}}$ from Padé continuation. A 4^2 discretization is employed. For each $\sigma_{\mathbf{Q}}$ shown, sum rule (3.20c) is satisfied at the 1% level. (a) $\mathbf{Q}=(\pi,\pi)$, (b) $\mathbf{Q}=(\pi/2,0)$.

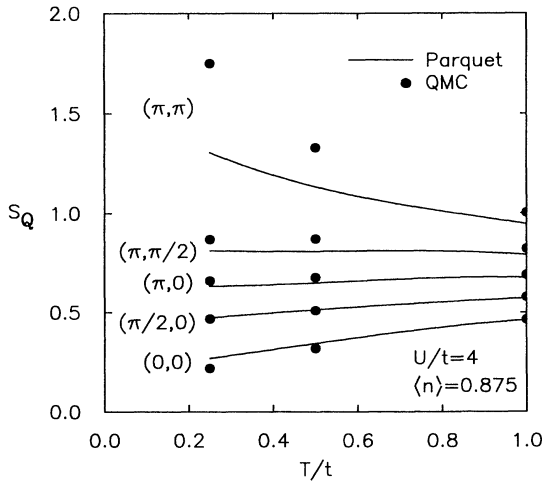

FIG. 40. Comparison of parquet and QMC results for the magnetic structure factor $S_{\mathbf{Q}}$ at $\langle n\rangle=0.875$. Agreement is almost quantative, except at $\mathbf{Q}=(\pi,\pi)$.

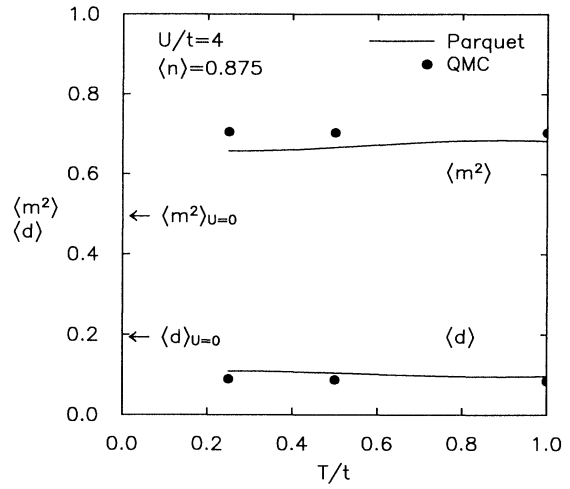

FIG. 41. Comparison of parquet and QMC results for the local moment $\langle m^2 \rangle$ and mean double occupancy $\langle d \rangle$ at $\langle n \rangle = 0.875$. The corresponding temperature-independent results for $U=0$ are indicated by arrows at the left.

IV. CONCLUSIONS

The principal conclusions to be drawn from this study of SCF approximations for the 2D Hubbard model are as follows: (i) the fluctuation exchange (FLEX) approximation introduced in I allows a semiquantitative description of one- and two-particle properties, and suggests a *d*-wave superconducting instability may occur near half-filling; (ii) the FLEX approximation may be viewed as the first nontrivial step in an iterative solution of parquet equations for models of this type; (iii) a pseudopotential treatment of irreducible particle-hole and particle-particle vertices allows a feasible approximate solution of the parquet equations; (iv) except at half-filling, the pseudopotential approach brings results for one- and two-particle correlation functions into nearly quantitative agreement with finite-lattice QMC simulations in the intermediate coupling limit.

A number of important questions remain for further investigation in this area. On the technical side, the robustness of the pseudopotential approximation must be more thoroughly examined. We have not studied in detail the dependence of results on the values of total momentum and energy chosen to define the pseudopotentials; nor have we mapped out the dependence of the irreducible vertices on relative momentum and energy. It would be desirable to carry out calculations using vertices which incorporate at least partial dependence on the *relative* variables, perhaps using a separable parametrization based on orthogonal functions. Some such extension of the present approach is certainly necessary to study systems with strong-*d* wave singlet and *p*-wave triplet fluctuations. An exact parquet solution for two-dimensional models must at present await further advances in computer power.

The approaches used here are clearly not limited to the two-dimensional repulsive-U Hubbard model. (i) There is interest in studying the repulsive Hubbard model in one and three dimensions: in one dimension exact results exist for a large number of thermodynamic properties and for the singular part of some dynamic correlation functions. Further, both QMC and SCF calculations require substantially less computer power in one dimension. While computer requirements are more severe in three dimensions, the benefit of calculations would be particularly great in this case: the majority of strongly correlated materials which have been described by Hubbard models are three dimensional. (ii) Interest has also been expressed in the behavior of the attractive-U Hubbard model.[35] In this case density and particle-pair fluctuations, rather than magnetic fluctuations, are expected to dominate the behavior. (iii) The simplest context for examining SCF approximations (particularly parquet solutions) in greater detail is provided by the Anderson impurity model[36] (effectively a zero-dimensional Hubbard model). In this case results for comparison are available from a wide variety of sources, including numerical renormalization group, Bethe ansatz and QMC studies. Furthermore, calculations require only a frequency variable, rather than both frequency and momentum. (iv) A simple electron-phonon model has been previously examined using the SCF approach.[37,38] Such models are of interest for potential competitions between *s*-wave superconductivity and Peierls and/or charge-density-wave order. (v) A variety of extended Hubbard models can be treated using the techniques developed in I and this paper. Note, however, that the fluctuation propagators which describe models with several bands or extended-range interactions are more complex than the Hubbard propagators, and computer requirements are substantially greater.

Finally, an important area for further study is the extension of the present techniques to the zero-temperature limit. For this purpose a method to single out Fermi surface behavior is required. One can imagine dividing the self-energy and irreducible vertices into parts corresponding to high and low frequencies (and momentum); then solving for low-frequency variables using "frozen" high-frequency variables, determined explicitly at higher temperature. The Anderson impurity model and one-dimensional Hubbard model provide natural testing grounds for future studies of this type.

ACKNOWLEDGMENTS

We acknowledge useful discussions with K. S. Bedell, D. L. Cox, K. F. Quader, R. T. Scalettar, and J. W. Serene. We especially thank D. J. Scalapino for stimulating discussions throughout the course of this work. This project was initiated at the Institute for Theoretical Physics in Santa Barbara and completed at the International Center for Theoretical Physics in Trieste. N.E.B. thanks both Institutes for their hospitality. This work was supported in part by the National Science Foundation under Grants Nos. DMR89-13850 (N.E.B.) DMR86-15454 (S.R.W.), and PHY82-17853 (N.E.B.); by the Office of

Naval Research under Grant No. N00014-90-J-1747 (N.E.B.); and by the Faculty Research and Innovation Fund at USC (N.E.B.). Most of the computer calculations were performed on the Cray X-MP and Y-MP at the San Diego Supercomputer Center. We thank SDSC for its support. This research was also supported in part by the University of California at Irvine through an allocation of computer time.

[1]See, e.g., G. R. Stewart, Rev. Mod. Phys. **56**, 755 (1984).
[2]J. G. Bednorz and K. A. Müller, Z. Phys. B **64**, 18 (1986).
[3]M. K. Wu, J. R. Ashburn, C. J. Torng, P. H. Hor, R. L. Meng, L. Gao, Z. J. Huang, X. Q. Wang, and C. W. Chu, Phys. Rev. Lett. **58**, 908 (1987).
[4]D. J. Scalapino, E. Loh, and J. E. Hirsch, Phys. Rev. B **35**, 6694 (1987).
[5]N. E. Bickers, D. J. Scalapino, and R. T. Scalettar, Int. J. Mod. Phys. B **1**, 687 (1987).
[6]A. E. Ruckenstein, P. J. Hirschfeld, and J. Appel, Phys. Rev. B **36**, 857 (1987); G. Baskaran, Z. Zou, and P. W. Anderson, Solid State Commun. **63**, 973 (1987).
[7]G. Kotliar, Phys. Rev. B **37**, 3664 (1988).
[8]D. J. Scalapino, *Frontiers and Borderlines in Many-Particle Physics* (Societa Italiana di Fisica, Bologna, 1988), p. 363.
[9]S. R. White, D. J. Scalapino, R. L. Sugar, E. Y. Loh, J. E. Gubernatis, and R. T. Scalettar, Phys. Rev. B **40**, 506 (1989).
[10]A. Moreo, D. J. Scalapino, R. L. Sugar, S. R. White, and N. E. Bickers, Phys. Rev. B **41**, 2313 (1990).
[11]N. E. Bickers and D. J. Scalapino, Ann. Phys. (N.Y.) **193**, 206 (1989).
[12]A. E. Ruckenstein and S. Schmitt-Rink, Phys. Rev. B **38**, 7188 (1988).
[13]C. de Dominicis and P. C. Martin, J. Math. Phys. **5**, 14 (1964).
[14]S. Babu and G. E. Brown, Ann. Phys. (N.Y.) **78**, 1 (1973).
[15]M. Pfitzner and P. Wölfle, Phys. Rev. B **35**, 4699 (1987).
[16]K. F. Quader, K. S. Bedell, and G. E. Brown, Phys. Rev. B **36**, 156 (1987), and references therein.
[17]G. Baym and L. P. Kadanoff, Phys. Rev. **124**, 287 (1961).
[18]G. Baym, Phys. Rev. **127**, 1391 (1962).
[19]For a more detailed derivation of the parquet equations in the context of lattice electron systems, see N. E. Bickers, in *Proceedings of the Adriatico Research Conference on Strongly Correlated Electron Systems,* edited by Yu Lu (World Scientific, Singapore, in press).
[20]L. G. Aslamazov and A. I. Larkin, Fiz. Tverd. Tela (Leningrad) **10**, 1104 (1968) [Sov. Phys. Solid State **10**, 875 (1968)].
[21]B. Roulet, F. Gavoret, and P. Nozières, Phys. Rev. **178**, 1072 (1969).
[22]See, e.g., J. Solyom, Adv. Phys. **28**, 201 (1979).
[23]N. F. Berk and J. R. Schrieffer, Phys. Rev. Lett. **17**, 433 (1966).
[24]E. Y. Loh, J. E. Gubernatis, R. T. Scalettar, S. R. White, D. J. Scalapino, and R. L. Sugar, Phys. Rev. B **41**, 9301 (1990).
[25]N. E. Bickers, D. J. Scalapino, and S. R. White, Phys. Rev. Lett. **62**, 961 (1989).
[26]The phase diagram published in Ref. 24 was obtained using an earlier version of our FLEX code. This code contained several interpolation routines which were less accurate than the procedure used here. This accounts for the small quantitative difference in results for eigenvalues and transition temperatures.
[27]The behavior of parquet equations in the vicinity of 2D Kosterlitz-Thouless transitions is an interesting unsolved problem, which we do not consider here. See also the discussion in H. J. Schulz, Europhys. Lett. **4**, 609 (1987).
[28]S. R. White, D. J. Scalapino, R. L. Sugar, and N. E. Bickers, Phys. Rev. Lett. **63**, 1523 (1989).
[29]M. Jarrell and O. Biham, Phys. Rev. Lett. **63**, 2504 (1989).
[30]R. N. Silver, D. S. Sivia, and J. E. Gubernatis, Phys. Rev. B **41**, 2380 (1990).
[31]H. J. Vidberg and J. W. Serene, J. Low Temp. Phys. **29**, 179 (1977).
[32]No magnetic sum rule analogous to Eq. (3.20a) appears, since σ_Q is an odd function of ω.
[33]We have not used QMC results for this purpose, since we wish to test only the reliability of the continuation at this point, not the overall quality of the approximation.
[34]To obtain local instantaneous correlations, it might be more efficient to solve the SCF equations directly in space and imaginary time.
[35]S. Schmitt-Rink, C. M. Varma, and A. E. Ruckenstein, Phys. Rev. Lett. **63**, 445 (1989).
[36]P. W. Anderson, Phys. Rev. **124**, 41 (1961).
[37]R. T. Scalettar, N. E. Bickers, and D. J. Scalapino, Phys. Rev. B **40**, 197 (1989).
[38]N. E. Bickers, Q. Luo, R. Noack, D. J. Scalapino, and R. T. Scalettar, unpublished.